Synthesis and Characterization of Dual-Metal Nanoparticle Catalysts for Plasma-Catalytic Ammonia Synthesis

Department of Chemical Engineering

McGill University

Dante St. Prix

A thesis submitted to McGill University

July 17, 2022

Abstract

The Haber-Bosch process, is the most common method of producing ammonia, a necessary ingredient of fertilizer. This technology leads to a substantial release of greenhouse gas emissions due to being powered mainly with fossil fuels, and using hydrogen generated from steam reforming, which produces CO_2 as a byproduct. Since constant energy is required, it is difficult to power using renewable sources. Plasma-catalytic ammonia synthesis is seen as a potential green alternative since it can be run intermittently. Additionally, a large amount of energy is required to attain the high pressures and temperatures at which the Haber-Bosch process operates. In contrast, plasma-catalytic ammonia synthesis can run near room temperature and atmospheric pressure. The main drawback is the lack of an effective catalyst, resulting in low energy efficiency making it currently uneconomical for commercial use. It is commonly accepted that catalysts consisting of two metals would most likely have the best performance. In this thesis, pulsed laser ablation is used to synthesize finely dispersed bimetallic nanoparticle catalysts on boron nitride nanotubes. The advantage of this method is the high catalyst stability and surface area. CoMo, FeRu and NiRu samples that were subjected to an argon plasma (1.22 W/cm^2), high-temperature (500˚C for CoMo and FeRu, 415˚C for NiRu) and both simultaneously are analyzed and imaged using XPS and SEM, to determine their stabilities in various working conditions. All metals except for Ru in as-prepared samples are found predominantly as oxides. A relatively minor change is seen when heat and plasma is applied separately. However, when both are simultaneously applied, a large increase in the elemental form of each metal is observed. A crust-like formation is found on a portion of the surfaces of these samples and that of heated FeRu using SEM imaging; as opposed to the well-defined nanotube structures generally found. This leads to a reduction in area, likely preventing the exposure to air of newly reduced metal species.

A calibration curve relating the number of laser shots to metal deposition is produced using results from ICP-AES. It is found that the ratio of metals deposited depends moderately on their minimum ablation energies calculated using their heat capacities, and heats of fusion and vaporization. Other factors include fractional ionization, and the amount of energy converted to kinetic energy of the ions, which is dependent on the properties of each metal. Sulfur contamination of unknown origin is found through both ICP-AES and XPS.

Abrégé

Le procédé Haber-Bosch est la méthode la plus courante de production d'ammoniac, un ingrédient nécessaire des engrais. Cette technologie entraîne une libération substantielle d'émissions de gaz à effet de serre en raison de son alimentation principalement avec des combustibles fossiles et de l'utilisation d'hydrogène généré par le reformage du méthane à la vapeur, qui produit du CO2 comme sous-produit. Étant donné qu'une énergie constante est nécessaire, il est difficile d'utiliser des sources d'énergie renouvelables. La synthèse catalytique par plasma de l'ammoniac est considérée comme une alternative potentielle car elle peut être exécutée par intermittence. De plus, une grande quantité d'énergie est nécessaire pour atteindre les pressions et températures élevées auxquelles le procédé Haber-Bosch fonctionne. En revanche, la synthèse d'ammoniac catalytique au plasma peut fonctionner près de la température ambiante et de la pression atmosphérique. Le principal inconvénient est l'absence d'un catalyseur efficace, ce qui entraîne une faible efficacité énergétique, ce qui le rend actuellement non économique pour une utilisation commerciale. Il est communément admis que les catalyseurs constitués de deux métaux auraient très probablement les meilleures performances. Dans cette thèse, l'ablation par laser pulsé est utilisée pour synthétiser des catalyseurs de nanoparticules bimétalliques finement dispersées sur des nanotubes de nitrure de bore. L'avantage de cette méthode est la grande stabilité du catalyseur et sa grande surface. Échantillons de CoMo, FeRu et NiRu qui ont été soumis à un plasma d'argon (1,22 W/cm2), à haute température (500˚C pour CoMo et FeRu, 415˚C pour NiRu) et les deux sont simultanément analysés et imagés à l'aide de XPS et SEM, afin de déterminer leur stabilité dans diverses conditions de travail. Tous les métaux, à l'exception du Ru dans les échantillons tels que préparés, se trouvent principalement sous forme d'oxydes. Un changement relativement mineur est observé lorsque la chaleur et le plasma sont appliqués séparément. Cependant, lorsque les deux sont appliqués simultanément, une forte augmentation de la forme élémentaire de chaque métal est observée. Une formation en forme de croûte se trouve sur une partie des surfaces de ces échantillons et celle de FeRu chauffé en utilisant l'imagerie SEM ; contrairement aux structures de nanotubes bien définies que l'on trouve généralement. Cela conduit à une réduction de la surface, empêchant probablement l'exposition à l'air d'espèces métalliques nouvellement réduites.

Une courbe d'étalonnage reliant le nombre de tirs laser au dépôt de métal est produite à l'aide des résultats de l'ICP-AES. On constate que le rapport des métaux déposés dépend

modérément de leurs énergies minimales d'ablation calculées à partir de leurs capacités calorifiques, et des chaleurs de fusion et de vaporisation. D'autres facteurs comprennent l'ionisation fractionnée et la quantité d'énergie convertie en énergie cinétique des ions, qui dépend des propriétés de chaque métal. Une contamination par le soufre d'origine inconnue est détectée à la fois par ICP-AES et XPS.

Acknowledgements

I am extremely grateful for having had the opportunity to develop many important skills ranging from teamwork to obtaining and organizing data. None of this would have been possible without the continuous support and guidance from my supervisor, Professor Sylvain Coulombe. I would also like to thank Dr. Elmira Pajootan for helping me learn to use the XPS, SEM and the laser setup; Steven Walker and Ranjan Roy for carrying out ICP-AES; Lizbeth Moreno Bravo for running the TPR experiments; and the CPPE group as a whole, for being there during the most isolating and chaotic months.

From the NRC, I would like to thank Ruilin Liang for the SEM images, and Dr. Benoit Simard and Dr. Ken Bosnick for providing insights into how to best work with BNNTs. It is thanks to the collaboration with the NRC that I was able to obtain the BNNTs, a novel material to which very few people have access.

While my parents live on the other side of this continent, they have been instrumental in grounding myself after several weeks to months living alone.

Table of Contents

List of Figures

List of Tables

Introduction

Ammonia (NH_3) plays a crucial role in food production as it is used to create synthetic fertilizer. The Haber-Bosch process involves the reaction of hydrogen (H_2) and nitrogen (N_2) and most commonly uses an iron catalyst. It is currently the most cost- and energy-effective technique employed to synthesize ammonia, consuming 27-36 GJ t-NH_3^{-1} [1], which is near the theoretical limit. However, because of the high pressures and temperatures required, the plants can only be efficient if run continuously and at a large scale. This makes it difficult to power using renewable sources as solar and wind for example do not provide continuous power; and battery technology is not yet capable of storing enough energy. As a result, fossil fuels are most often used to power NH_3 synthesis reactors [1]. Fossil fuels are also used to produce the vast majority of hydrogen produced worldwide. In 2020, 76% of worldwide H_2 production was through steam reforming, a reaction that consumes methane (CH_4) to produce carbon monoxide (CO), which is processed further to produce carbon dioxide (CO_2). Coal gasification, a more energy intensive process, accounts for 22% of global production (due to widespread use in China) [2]. Overall, 1-2% of global greenhouse gas emissions are generated from the production of ammonia [3].

The goal is to develop technologies to electrify the aforementioned processes. Hydrogen can already be produced using electrolysis [1]. The Haber-Bosch process itself can be electrically driven with ohmic heating and electric compressors. However due to the intermittent nature of renewable sources, this is not feasible in most places [4]. Technologies such as plasma-catalytic synthesis are being developed with the aim of eliminating the need for high temperatures and pressures in ammonia production, which will in turn allow for intermittent operation. This will favor the decentralization of ammonia production and likely prove beneficial for the food security of regions that lack the capital required for large-scale operations. In addition, there is considerable interest in green technology of this kind as an increasing number of countries are committing to net-zero emissions by 2050. Not only will this enable cleaner production of fertilizer but also the possible use of ammonia as a hydrogen storage vector and a carbon-free fuel. Selecting an effective catalyst is crucial as it determines the conversion. In a later section, it will be explained how much of the difficulty in discovering an optimal catalyst is due to activity being dependent on two competing processes [1], in which it is required to achieve a balance. While certain metals such as ruthenium are fairly effective, no single metal is optimal. If two metals are combined, it is expected

that such bimetallic catalyst will be much closer to the optimal point [5]. Another factor to be considered is geometry and morphology. It is well-known that increasing the surface area of a catalyst by decreasing the particle size maximizes activity. Nanoparticles (NPs) with an average diameter of 4 nm have been successfully deposited onto support structures using pulsed laser ablation (PLA) [6]. In this thesis, I will be producing samples using PLA to determine the amount of metal deposited per laser pulse. This will be followed by synthesizing samples and determining their chemical states and morphologies.

Background

Non-thermal plasma catalytic synthesis of Ammonia

Non-thermal plasma catalytic synthesis is an alternative to the Haber-Bosch process. Plasma, which is known as the fourth state of matter consists of "electrons, positive and negative ions, photons, radical, and neutral atoms and molecules in ground state or excited in vibration or electronic modes" [1] can be ignited and sustained using electrical energy. Plasmas are of great interest because species can exist with degrees of freedom not in equilibrium [7]. In particular, non-thermal plasmas contain electrons at very high temperatures (~10^5K) with bulk gases near room temperature and can exist below atmospheric pressure [8], resulting in a much lower energy expenditure compared to the Haber-Bosch process.

Plasma-catalysis of ammonia involves supplying the required breakdown voltage between two electrodes separated by nonconducting gases, which ionize due to collisions with electrons [1]. The dielectric barrier discharge reactor (DBD) is most commonly used for plasma catalytic synthesis of ammonia since it functions at atmospheric pressure [1]. In DBD reactors, an AC current at a high voltage with a frequency ranging from 0.05 – 500 kHz, or a DC pulse is applied to two electrodes separated by a dielectric barrier (most commonly quartz, glass, or alumina) [8]. Discharges, known as filaments or streamers occur only between the two electrodes [1]. The interaction between the catalyst and filaments increases the electric field strength, producing a plasma in non-equilibrium [8]. To avoid interacting with the electric field, it is preferable for the catalyst to be an insulator [8]. In terms of the placement of the discharge region, several configurations have been implemented as shown in Figure 1 [9]. In a single-stage reactor, the catalyst is in contact with the plasma whereas in the double-stage reactor, the reactants reach the catalyst after interacting with the plasma. The configuration is chosen depending on the characteristics of the reaction and catalyst. For example, O_3 assisted CO oxidation requires a double-stage reactor as ozone is first produced in the discharge region. Figure 2 shows an example of a packed-bed DBD reactor used for ammonia synthesis [10] with the electrodes being arranged concentrically.

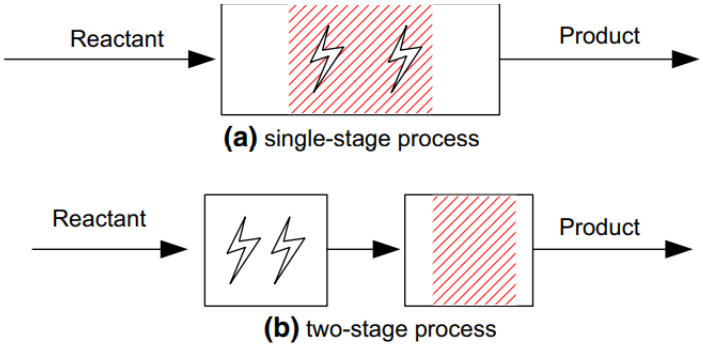

Figure 1: Two configurations for the DBD reactor. (a) Is a single-stage reactor with catalyst in contact with plasma, and (b) is a double-stage reactor with catalyst downstream from plasma [9]

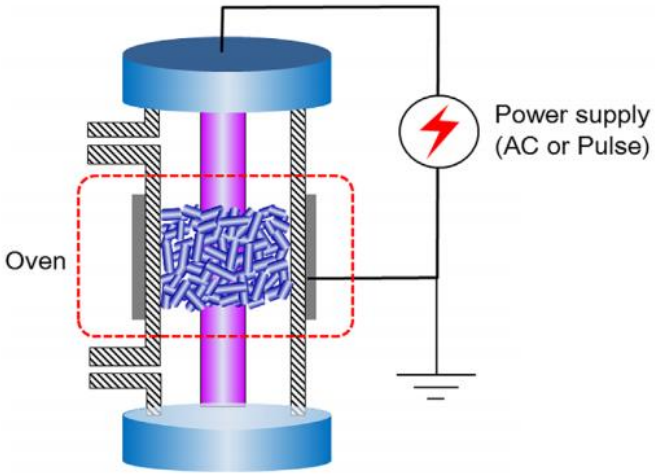

Figure 2: Packed-bed single-stage DBD reactor used for plasma synthesis of ammonia [10]

Researchers have also synthesized ammonia using radio-frequency (RF) plasmas, microwave (MW) and glow discharges [1]. An RF plasma is produced by alternating the polarity of each electrode at RF frequencies, allowing it to reach non-equilibrium, a state in which the electron temperature is much higher than the bulk temperature [11]. The electrons accelerate significantly every cycle allowing more impact with gas molecules and higher rates of ionization

compared to a direct-current (DC) plasma [1]. The MW and glow discharges operate with microwaves and DC currents being applied, respectively.

Based on the performances of reactors developed by various researchers, DBDs appear to be the most efficient. These results are summarized in Figure 3 [1], which shows a plot of their energy yields and ammonia concentrations. A high enough ammonia concentration (1000 ppm) is required for ammonia separation using solid sorbents [1]. As of 2020, the highest energy yield obtained is 37.9 g-NH_3/kWh. Kim et al. [10] calculated that to be competitive, an energy yield of 150 – 200 g-NH_3/kWh should be achieved. Thus, much improvement must be made before plasma catalytic synthesis of ammonia can become commercially viable at an industrial scale.

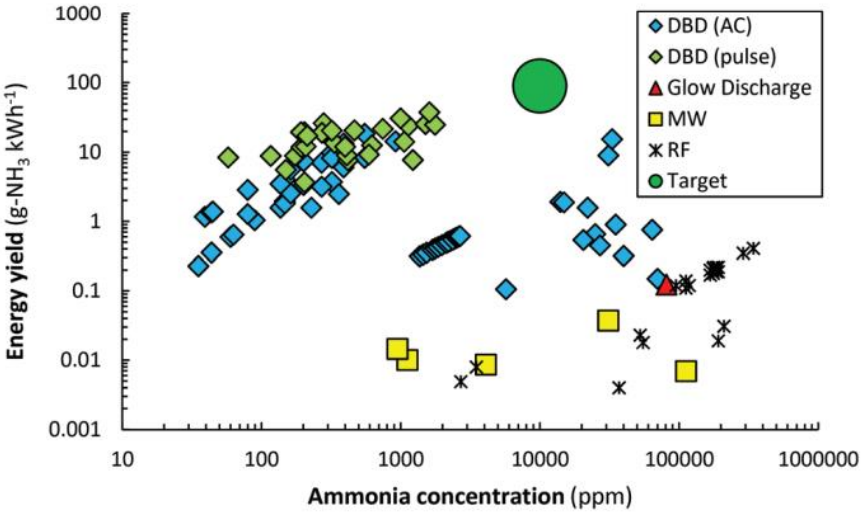

Figure 3: Energy yield plotted against ammonia concentration with various experimental setups [1]

Reaction Pathway

While various feedstocks have been explored, such as CH_4 and N_2, we will only consider N_2 and H_2 since using the former can inadvertently form undesirable compounds like hydrogen cyanide [1]. Thus, the reaction mechanism for ammonia synthesis (with an iron-catalyst) is as follows [1]:

1) $H_2 + 2e^- \leftrightharpoons 2H^-$ (Rx. 1)

2) $N_2 + 2e^- \leftrightharpoons 2N^-$ (Rx. 2)

3) $N^- + H^- \leftrightharpoons NH^- + e^-$ (Rx. 3)

4) $NH^- + H^- \leftrightharpoons NH_2^- + e^-$ (Rx. 4)

5) $NH_2^- + H^- \leftrightharpoons NH_3^- + e^-$ (Rx. 5)

6) $NH_3^- \leftrightharpoons NH_3 + e^-$ (Rx. 6)

where the rate determining step is 2) N_2 dissociation, the breaking of the triple N≡N bond. The plasma provides the necessary dissociation energy with electron energies found to be in the range of 0.01 – 16 eV [8], with the energy of the N≡N bond being approximately 9.8 eV [12]. In the Haber-Bosch process, this energy is introduced by using high temperatures [1]. In a recent study by Rouwenhorst et al. [11] comparing thermal catalysis and plasma catalysis, it was confirmed that a linear correlation exists between the inverse of temperature and the natural logarithm of the activity for the thermal catalysis. For plasma catalysis, no such correlation was found, and for the same catalysts the activity was found to constantly be at the upper limit of what can be done thermally. This supports the idea that the plasma can supply the activation energy.

Several researchers have proposed various reaction pathways for reactors at atmospheric pressure [13, 14, 15, 16]. This is important as it dictates which catalytic properties are required to produce the best results. For example if N_2 dissociates in the gas-phase, as proposed by Peng et al. [13], then the catalyst would not need to facilitate this initial reaction and atomic nitrogen can be regarded as part of the feedstock. They suggested that H_2 also dissociates before reacting with nitrogen to form NH, still in the gas-phase. NH and hydrogen undergo adsorption and react on the surface to form ammonia. According to Hong et al. [14], the most important factor governing the rate of this reaction would be the concentration of atomic hydrogen. Conversely, Mizushima et al. [15] proposed that nitrogen undergoes dissociative adsorption on the catalyst; the step that Mehta et al. [16] considers the rate determining step. Thus, the catalyst would be required to have a high nitrogen adsorption energy. Other considerations include nitrogen and hydrogen recombination [17] and ammonia decomposition [18] among others. It is important to note that the above researchers used varying but mainly rudimentary catalyst configurations in their analyses. It is

expected that each configuration would give rise to diverse reaction mechanisms, perhaps differing to the point where some follow the Langmuir-Hishelwood (L-H) mechanism where both molecules adsorb before reacting and others follow the Eley-Rideal (E-R) mechanism, where only one reactant adsorbs, while the other remains in the gas phase. A thin bimetallic coating on a nanomaterial support for example would add a high degree of complexity as the plasma, feedstock, the two metals, and the support would all interact in ways that are difficult to predict and measure.

It will be assumed that the proposal by Mizushima et al. [15] takes place since it was discovered that the activity is related to the adsorption energy of nitrogen as shown in the 'volcano curve' in Figure 4 [1]. When nitrogen binds too strongly to the catalyst, the molecules easily dissociate but cannot easily be released from the catalyst, impeding ammonia desorption. This phenomenon can be seen to the left of the peak. On the right side, the catalysts cannot effectively dissociate nitrogen molecules, resulting in a lower activity. The best catalysts are found near the peak, where dissociation and desorption can both proceed with relative ease. Ruthenium, osmium,

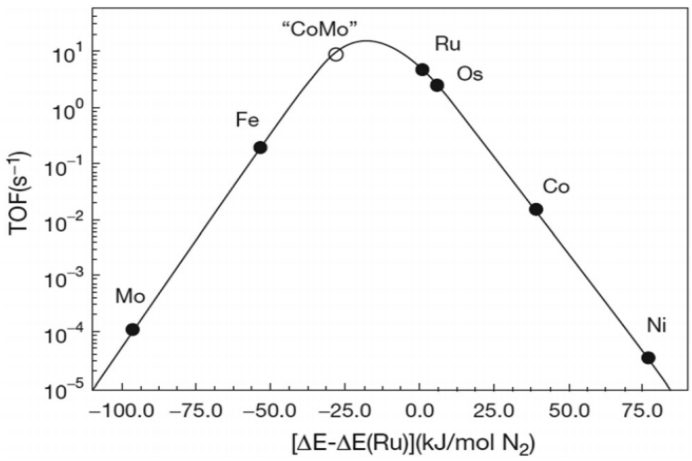

Figure 4: Ammonia synthesis turnover frequency as a function of nitrogen adsorption energy at 400°C and 50 bar [5]

and to a lesser extent iron are the most suitable catalyst materials. An interesting candidate is the bimetallic cobalt-molybdenum catalyst. Yazdi et al. [19] performed a DFT study for a Co_3Mo_3N surface. Nitrogen vacancies were introduced as they had previously found that they result in an 11% activation (the percent reduction of the N≡N bond length). Their simulations show how the reaction may follow distinct L-H and E-R mechanisms, as illustrated in Figure 5. The L-H

mechanism begins with N_2 adsorbing on the catalyst (A) and dissociating, creating "two bridged-N intermediates" (B). H_2 dissociates at a Co_8 cluster to form atomic hydrogen (C), which reacts with a bridged-N intermediate to form azane (NH) (D). This further reacts at the interface between Co and Mo to form NH_2 (E). An additional H_2 dissociates at a Co_8 cluster (F). The other bridged-N intermediate takes the position of the NH_2 (G) to react with H to form NH (H, I). A final H_2 dissociates at a Co_8 cluster (J), and reacts with the NH to form NH_2 (K), which further reacts with H to form NH_3 (L) before desorbing (M), allowing the process to restart from (A).

The E-R mechanism involves N_2 adsorbing at a nitrogen vacancy (A'), which reacts with hydrogen in the gas phase to form an NNH_2 intermediate (B'). H_2 adsorbs onto Mo_3N, next to the NNH_2 intermediate (C'). The two species react to form diazine (D'), which decomposes to a tertiary amine (E'). This amine reacts with hydrogen (the other one of the two atoms in molecular hydrogen) to create azane (NH) (F'). An additional H_2 adsorbs (G'). One H reacts with NH to form a primary amine (H'). This in turn reacts with the other H to form NH_3 (I'), which dissociates, finishing the process (J'). Calculations by Yazdi et al. [19] suggest that the E-R mechanism will

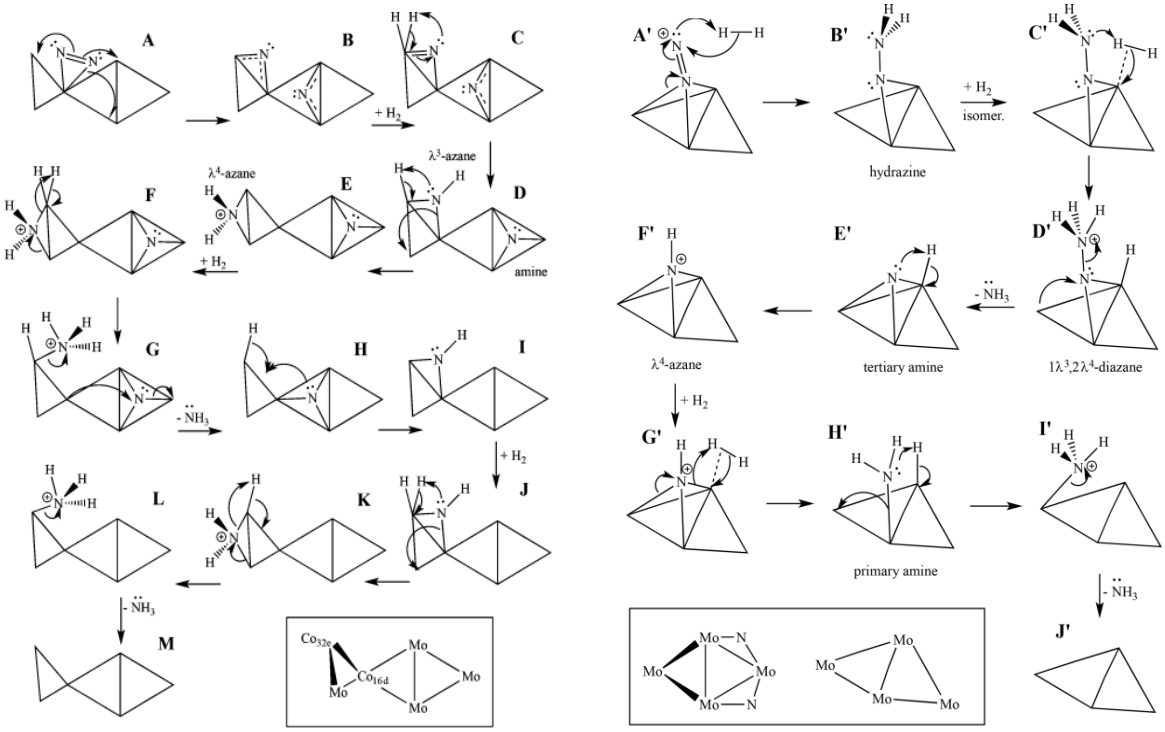

Figure 5: L-H mechanism (left) and E-R mechanism (right) pathways proposed by Yazdi et al. [19] for NH_3 synthesis using a CoMo catalyst.

have a significantly lower activation energy and can thus operate at lower temperatures. This mechanism requires nitrogen vacancies however, and will not proceed with a CoMo catalyst without N. Thus, for this catalyst, it is more likely for the reaction to follow a L-H mechanism.

No similar analysis has been done to this date on the reaction mechanism involving a bimetallic catalyst in a plasma-catalytic reactor. In conclusion, it is not possible at this point to deduce which catalyst would have the highest activity, and the amount of ammonia yielded, so it is required to evaluate each catalyst experimentally. The following section discusses practical considerations when synthesizing effective catalysts.

Single-Metal Catalysts

When designing a catalyst, one major consideration is maximizing the surface area, and minimizing particle size to promote its activity. Metal catalysts are loaded onto a support, which increases the surface area since the support materials generally have high porosities (Al_2O_3, SiO_2) [20]. The resultant catalyst pellet is generally in the mm scale. Another consideration is the support's stability, or its ability to resist high temperatures and reactive environments. Methods to prepare catalysts include impregnation, coprecipitation and the sol-gel process [20]. Plasma treatment can later be applied to decrease the particle size, improve dispersion, and reduce the catalysts [20]. One benefit of this, for example, is that plasma-treated catalysts used in dry reforming of methane, produce significantly less water compared to untreated ones [20].

A promoter is a material added in small quantity to the catalyst to facilitate the reaction. Using FTIR analysis, it was discovered that certain promoters like MgO increases the rate of electron transfer between the support and promoter, and the N_2 molecule [21]. Thus, most catalysts found in studies and used in industrial ammonia production include all three components.

In the study by Rouwenhorst et al. [11], the activity of $2Ru/\gamma\text{-}Al_2O_3$ (ruthenium on aluminum oxide supports) catalysts with various promoters was studied. It was concluded that for both thermal and plasma catalysis, the activity increases with decreasing electronegativity of the support and promoter. This observation, and several others in this study are important as they may indicate that non-thermal plasma catalysis may involve similar reaction pathways to the better characterized process of thermal catalysis. Nevertheless, it was suggested in [1] that plasma excitation can allow new pathways that are not otherwise thermodynamically possible.

Metal NPs loaded onto a nanotube forest would provide an even larger surface area. In addition, Gorky et al. [3] suggested "nanoparticles smaller than ~10 nm to exhibit unique electronic, optical, and magnetic properties due to the quantum mechanical effects." While it is difficult to theoretically predict the exact performance, experimental data yielded promising results. McArthur et al. [6] found that carbon nanotubes (CNTs) decorated with nickel NPs with an average diameter of 4 nm exhibited an activity two orders of magnitude higher than that of a solid nickel catalyst for the hydrogen evolution reaction.

If too much material is coated on the nanotube support, agglomeration occurs and results in larger particle sizes with higher surface area and reduced activity [6]. A catalyst with low thermal stability can become less effective when operated at elevated temperatures over time due to sintering from migration of NPs [22]. It is important to assess the materials for the catalyst support and active medium, and the preparation method with the goal of minimizing these effects.

Boron Nitride Nanotube Supports

Boron nitride nanotubes (BNNTs) comprise of cylindrical hexagonal sheets of alternating boron and nitrogen atoms [23]. Among other advantages compared to CNTs, BNNTs can withstand harsher chemical environments [22] such as plasmas, are stable in air up to around 900^{o}C [23] and are electrical insulators [24]. Finally, this material possesses extraordinary mechanical properties. For example, using a MEMS device, Arenal et al. [25] found that the Young's modulus for single-walled BNNTs exceed 1000 GPa. Currently, the NRC uses the hydrogen-assisted BNNT synthesis method to produce highly crystalline nanotubes with lengths of a few micrometers and diameters of no more than 15 nm; with the average diameter being 5 nm. Most BNNTs produced have 2 - 5 walls [26]. This was a particularly large milestone in the development of BNNT technologies as nearly 20 g/h of this material was produced; which is more than a 100-fold increase in production rate compared to previous methods used to produce BNNTs of a similar quality [26]. A 20 cm long yarn produced using this method was found to only have a Young's modulus of approximately 0.5 GPa [26], reflecting the difficulties encountered when producing macroscopic structures of nanomaterials.

Kim et al. [22] studied the deposition of Pt and Pd NPs using sonication on relatively large BNNTs with diameters of 30 – 50 nm and lengths exceeding 10 μm. Figure 6 shows the TEM

image of BNNTs decorated with Pd NPs with a loading of 2 wt % with each NP ranging in size from 2 - 3 nm. The NPs, which are seen as dark spots on the lighter nanotube, appear to be finely dispersed. Figure 7 [22] shows the XRD patterns of untreated and acid-treated BNNTs, and BNNTs coated with Pt and Pd. Acid treatment lead to the reduction in the amount of impurities such as MgO (interestingly, since MgO is known as a good promoter for conventionally-prepared catalysts, it is possible that catalysts for ammonia synthesis using their BNNTs would perform better without acid treatment). Since the h-BN peak at around 26.5˚ did not shift, Kim et al. [22] concluded that their BNNTs are unaffected by its exposure to 3 M HCl at room temperature (exposure time not specified) and 1 M HNO_3 at 90˚ C for 3 h. A small PdO peak can be found in the Pd decorated sample whereas no peaks corresponding to platinum were found in the Pt decorated sample.

NP migration was tested under varying temperatures for 2 h in air at atmospheric pressure. The results are shown in Table 1. At 400^{o}C, The Pd NPs remained unchanged whereas the Pt NPs started growing. However, the BNNT structure exhibited no visible change even at 800^{o}C. Thus, the selected metal rather than the BNNT support are the limiting factor when determining thermal stability. Further research should be undertaken to understand stability over thousands of cycles.

The thermal stability may also be impacted by the preparation method. The sonication method used by Kim et al. [22] to decorate the BNNTs with NPs works by immersing BNNT powder into a mixture of liquid solvents such as H_2PtCl_6 and HCl followed by centrifugation,

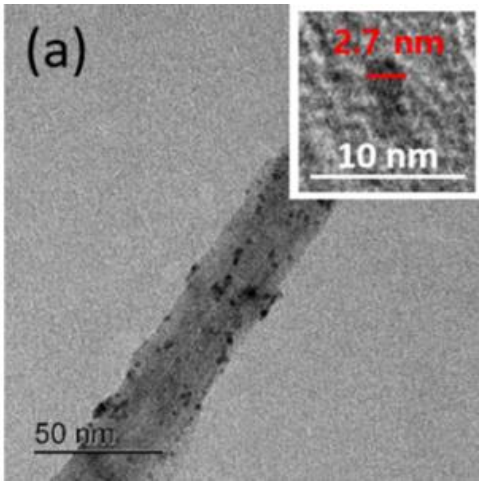

Figure 6: The TEM image of 2 wt % Pd-BNNT [22]

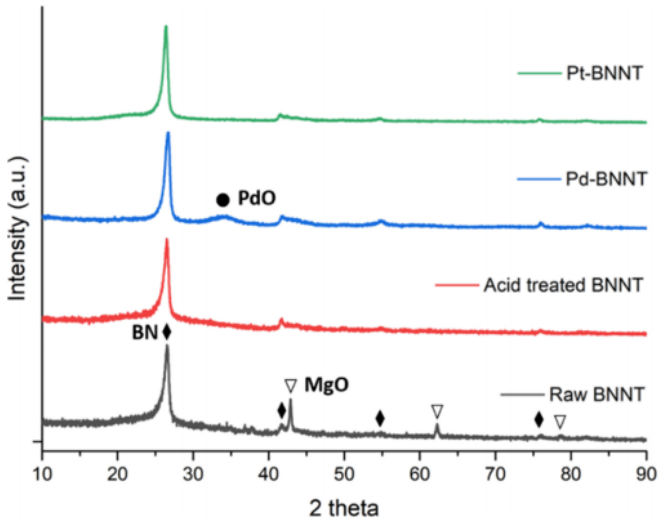

Figure 7: The XRD patterns of 2 wt % Pt-BNNT, 2 wt % Pd-BNNT, acid treated BNNT and raw BNNT [22]

rinsing, and drying on the hot plate. This handling can lead to the accidental introduction of impurities. Generally, it is difficult to control the number of NPs deposited and if a bimetallic catalyst is desired, it would be unrealistic to expect to deposit the desired ratio. Furthermore, large volumes of solvent waste are produced; something that is generally harmful for the environment if not properly disposed of.

Temperature	Pd Particle Size (nm)	Pt Particle Size (nm)
Room Temperature	~2-3	~1-2
400°C	~3	~3
600°C	~5	~4.5
800°C	~13	~9

Table 1: Particle sizes of Pd and Pt NPs in 2 wt % Pd-BNNT and 2 wt % Pt-BNNT after exposure to various temperatures [22].

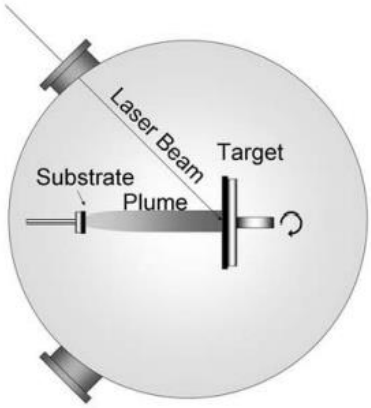

Figure 8: A schematic of the standard PLA setup [27]

Pulsed Laser Ablation

Pulsed laser ablation (PLA) involves the rapid vaporization of a target material using a pulsed laser in a low-pressure chamber. This generates a rapidly expanding plume [27], which upon condensation produces a thin coating on a nearby substrate. Since the 1980s, this technique has been used extensively by researchers in many fields due to its ability to deposit a wide range of materials including metals and various other crystalline materials such as metals and diamond-like carbon [28]. The synthesis of high-temperatures superconductors was an early application of PLA due to the need for complex structures involving oxide thin films, which are particularly difficult to grow because of the specific conditions required. This limitation was rendered irrelevant using PLA as the stoichiometry of the target is maintained, allowing any arbitrary oxide thin film to be produced [28] in a relatively short amount of time. Since a single laser pulse only deposits a fraction of a single atomic layer on the substrate surface, and supersaturation of the plume deposits NPs [6], PLA is ideal for producing finely dispersed metallic NPs on BNNTs. The setup used in this thesis is similar to the one shown in Figure 8 [27].

The two-temperature diffusion model describes the energy transfer from the laser to the free electrons in the target [29]:

$$C_e \frac{\partial T_e}{\partial t} = -\frac{\partial Q(z)}{\partial z} - \gamma(T_e - T_i) + S$$

$$C_i \frac{\partial T_i}{\partial t} = \gamma(T_e - T_i)$$

$$Q(z) = -\frac{k_e \partial T_e}{\partial z},\ S = I(t)A \propto e^{-\propto z}$$

where the subscripts e and i refer to the electron and lattice subsystems respectively. T_e and T_i refer to their temperatures and C_e and C_i are their heat capacities. Q(z) is the heat flux with z being perpendicular to the surface. The coupling between electronic excitations and lattice vibrations is known as electron-phonon coupling [30] and the strength of this phenomenon is represented by γ. S is from laser heating and is found by multiplying its intensity I(t) with the target's transmittance A and absorption coefficient α with the exponential factor arising from the wave equation. k_e is the thermal conductivity of the electrons. For the case of nanosecond laser pulses, the lattice heats up on a much faster timescale than the laser pulse. Thus, if we assume that $T_e = T_i$, then the equations can be condensed to [31]:

$$C_i \frac{\partial T_i}{\partial T} = \frac{\partial}{\partial z}\left(k_e \frac{\partial T}{\partial z}\right) + S$$

One parameter used in determining the effectiveness of a laser is its fluence F, which is defined as the energy per pulse divided by the area illuminated [31]. The concept of threshold fluence, or the minimum fluence required to ablate a material, arises due to energy loss via conduction to the target bulk which occurs during the time spent to melt and evaporate the metal. The threshold fluence, according to [29], follows this relationship:

$$F > F_{th} \sim \rho \lambda_e \sqrt{D} \times \sqrt{\tau_L}$$

where ρ is the target density, λ_e is the heat of vaporization, D is the heat diffusion coefficient and τ_L is the characteristic time scale of the laser pulse. Unlike the nanosecond pulse, very little energy is lost to the bulk when a femtosecond pulse is applied since the process occurs almost instantly, greatly reducing F_{th}.

Assuming that the threshold fluence is provided and negligible heat is lost to the bulk, the ablation rate is predicted to be proportional to the sum of the energy required to raise the metal to

its boiling point, melt and vaporize it. Table 2 refers to this as the minimum ablation energy. However, this is likely not exactly the case as the metal may heat beyond its boiling temperature or ionize, resulting in higher energy consumption. Faster conduction may reduce these effects. Thus, depending on many factors such as the pulse duration, target material and fluence, increased heat diffusion may either lead to higher or lower ablation rates. The rate at which heat diffuses in a material is the thermal diffusivity α:

$$\alpha = \frac{k}{\rho c_p}$$

where k is the thermal conductivity, ρ is the density and c_p is the specific heat capacity. Table 2 contains the minimum ablation energy in terms of both energy divided by mass and by volume. Since the ablation rate is generally in units of volume of metal vaporized divided by time, the minimum ablation energy in terms of volume is applicable when inferring relationships between the two. Based on these values, almost four times the volume of indium is expected to be ablated compared to nickel when an equal number of laser shots are applied.

Preuss et al. [32] studied the ablation rates of various metals illuminated with a 248 nm (UV) laser with a pulse width of 0.5 ps. This was done by measuring the depth of craters produced after ablation. Their results confirm the hypothesis of indium having the highest ablation rate with their plot of the ablation rate vs fluence at approximately 10^{-8} bar (1.3×10^{-6} Pa) shown in Figure 9 (left) [32]. This plot also demonstrates that each metal has a unique threshold fluence. Interestingly, the slope appears the steepest near the ablation threshold and decreases as fluence is increased, which may be due to more heating beyond the boiling point and ionization as the fluence is increased. Figure 9 (right) compares ablation rates of samples placed in vacuum and atmospheric pressure. It was found that while the threshold fluence remains constant, the ablation rate is much lower in air. According to the explanation provided by Preuss et al. [32], this is due to rapid condensation and redeposition. While the spot size is different with In and Ni spots for example having diameters of 200 and 400 μm respectively, the authors state that the ablation rate is independent of spot size because of negligible heat conduction occurring due to the short timescales involved with the use of a ps laser. It is noted that this is not be the case for ns lasers.

Metal	Boiling Point (K)			Heat Capacity (J/kg K)	Heat of Fusion (kJ/kg)	Heat of Vaporization (kJ/kg)	Minimum Ablation Energy (kJ)		Thermal Diffusivity (mm^2/s)
							per kg	per cm^3	
Fe	3134			449	247.1	6214.2	7736.9	60.9	22.3
Ru	4423			238	254.3	5738.6	6975.8	86.3	40.8
Mo	4912	251	375.2	6253.3	7787.8	80.1	53.9		
Co	3200	421	274.9	6363.5	7862.2	70.0	26.7		
Ni	3186	445	293.1	6440.6	8021.0	71.5	23.0		
Al	2792	904	396.6	10859.9	13515.4	36.5	96.3		
Cu	2835	384	206.1	4721.0	5904.2	52.9	116.1		
Pt	4098	133	102.5	2511.7	3120.3	66.9	24.9		
In	2345	233	28.4	2003.2	2509.6	18.3	48.1		
W	5828	132	190.4	4351.6	5272.6	101.5	66.9		

Table 2: Thermal properties of various metals [33]

The wavelength influences how the laser interacts with the target material. Torrisi et al. [34] ablated copper using 1064 nm (Nd:YAG fundamental frequency, 9 ns pulse width, ~10^{-7} mbar) and 308 nm (XeCl excimer, 20 ns pulse width, ~10^{-6} mbar); the former being in the IR range and the latter being a UV laser. The UV laser was found to have a much lower threshold fluence at 3 J/cm^2 compared to 7 J/cm^2 for the IR laser. To explain this, it is necessary to consider the absorption depth, Z, the depth at which the laser penetrates the surface [34]:

$$Z = \sqrt{\frac{2}{\omega \mu_0 \sigma}} + \sqrt{\alpha \tau}$$

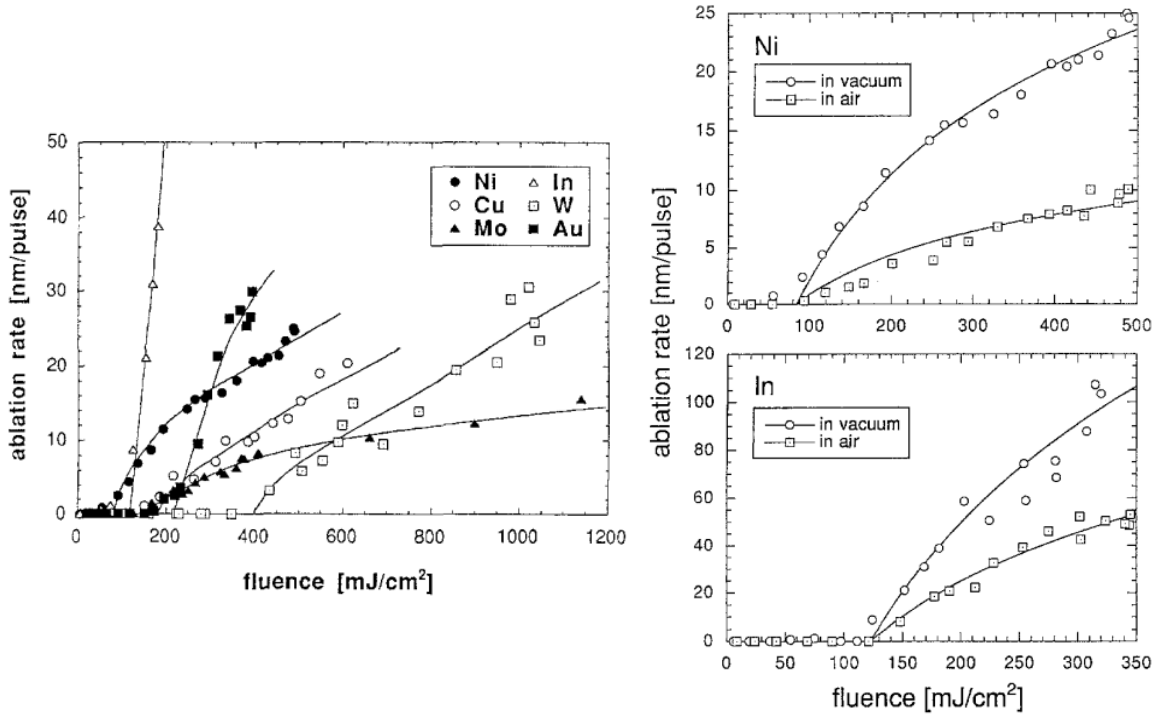

Figure 9: Ablation rates of a various metals in vacuum as a function of fluence (left), and the ablation rates for Ni and In in vacuum and air (right) with a sub-picosecond UV laser [32]

where ω is the angular frequency of the laser, μ_0 is the vacuum permeability, σ is the electrical conductivity, and τ is the pulse width. The first term in the equation is known as the skin depth and the second is the thermal diffusion length [34]. The latter term dominates with values of 1.4 and 2.2 μm for IR and UV lasers respectively compared to skin depths on the order of nm's [34]. Z multiplied by the spot size, S_0, and density provides the irradiated mass, m. Finally, the threshold fluence is given as [34]:

$$F_{th} = \frac{m}{S_0} \times \frac{c\Delta T + \lambda_f + \varepsilon\lambda_e}{1 - R}$$

where ΔT is the difference between the temperature of the chamber and the boiling temperature, λ_f is the heat of fusion, λ_e is the heat of vaporization, ε is the proportion of m that vaporizes, and R is the reflectivity at the boiling point. This equation is consistent with the initial description of F_{th} [29] in that both state that F_{th} is proportional to the square root of the pulse width while expanding upon it to consider both the thermal diffusivity and the minimum ablation energy

(which is equivalent to $c\Delta T + \lambda_f + \varepsilon\lambda_e$ when $\varepsilon = 1$) in a single equation and add a contribution from the material's reflectivity. R is given as [34]:

$$R = 1 - \sqrt{\frac{8\omega\varepsilon_0}{\sigma}}$$

where ε_0 is the vacuum permittivity. Torrisi et al. [34] calculated R to be 0.14 and 0 for the IR and UV laser respectively. This means that the surface will absorb nearly all of the UV radiation as opposed to 86% of the IR radiation. The threshold fluence was calculated to be 5.1 and 2.3 J/cm^2 for IR and UV respectively [34], with the ratio being 2.21. This was done by setting $\varepsilon = 0$, representing threshold conditions. This contrasts with the description of F_{th} from [29], which includes the heat of vaporization but not the heat of fusion. The ratio between the experimental values of 7 J/cm^2 and 3 J/cm^2 is 2.3, which is nearly identical, indicating that for this specific dataset, this physical explanation provides an accurate description. Other factors that were not considered likely account for the higher experimental threshold fluence value. These include surface roughness and inhomogeneous heating among others.

Despite having a lower threshold fluence, in the same study, Torrisi et al. [34] found that the ablation yield, defined as the number of copper atoms or ions ejected per laser pulse, increases more rapidly for the IR laser compared to the UV laser as shown in Figure 10 (top) [34]. The researchers also measured the ion current using a Faraday cup to indicate the extent at which copper ionization occurs. Figure 10 (bottom) [34] shows their results. Ionization also begins at the threshold fluence and increases linearly with fluence within 10 J/cm^2 of the F_{th}. The slope is greater for the UV laser compared to the IR one. In the case of the UV laser, the first four charge states were discovered but the majority of ions consisted of Cu^{2+} and Cu^{+}, with a 1:2 ratio. The ratio for IR laser is 1:15, with no higher charge states reported. The fractional ionization at a fluence of 10 J/cm^2 (proportion of ablated atoms ionizing) is 0.09 and 0.36 for the IR and UV lasers respectively [34]. The ionization energies of various metals is shown in Table 3 [33]. The first and second ionization energies for Cu in units of kJ/mol are 2.5 and 6.5 times the vaporization energy, respectively. Thus, even a small increase in the ionization will lead to a drastic decrease in ablation yield, explaining the greater ablation yield slope for the IR laser.

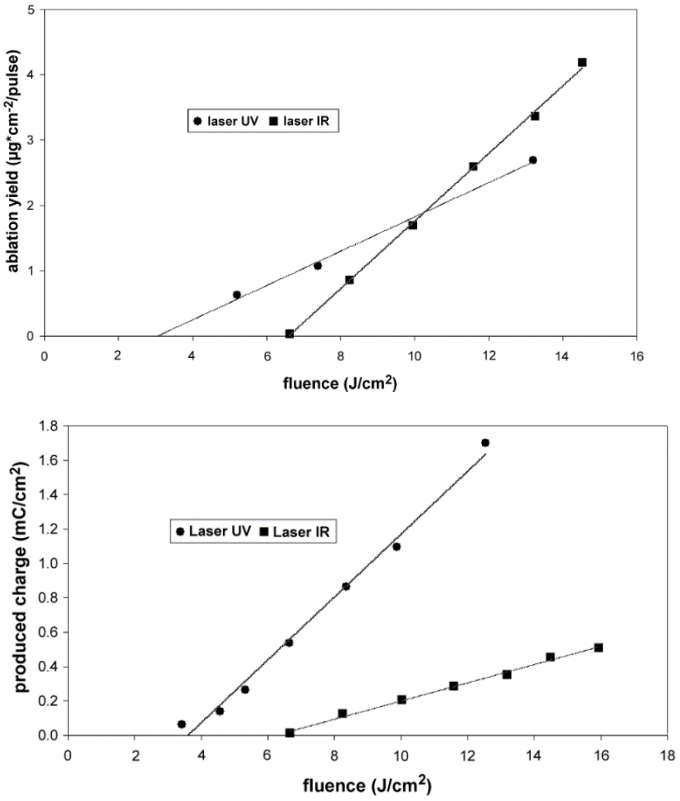

Figure 10: The ablation yield of copper (top) and charge produced (bottom) as a function of fluence for UV and IR lasers [34]

In another study by Torrisi et al. [35], various metals were illuminated using the same IR laser and the fractional ionization was measured; with the results shown in Table 4 [35]. There is a large variation in fractional ionization values, especially near the threshold fluence. According to Torrisi et al. [35], metals with low ionization energies and melting points ionize the most. Indeed, Pb, with the lowest first ionization energy (in units of kJ/cm^3) and the second lowest melting point has the highest ionization fraction near F_{th}. This correlation appears to hold true for the metals in the study.

After ionizing, additional energy is converted to kinetic energy (KE). Using time-of-flight measurements, Torrisi et al. [34] calculated the average Cu ion velocities at a fluence of 10 J/cm^2 with the values being 4.7×10^4 (916 eV) and 2.3×10^4 m/s (202 eV) for the IR and UV lasers, respectively. Accounting for the fractional ionization values provided (0.09 for IR, 0.36 for UV), and assuming neutral Cu has a relatively minuscule KE, 1121.4 and 989.1 kJ/cm^2, for the IR and UV lasers respectively, is converted to KE. This means that more energy is converted to KE than

Metal	First Ionization Energy		Second Ionization Energy		Melting Point (K)
	kJ/cm^3	MJ/kg	kJ/cm^3	MJ/kg	
Fe	107.5	13.6	220.2	27.8	1811
Ru	86.9	7.02	198.3	16.0	2607
Mo	73.3	7.1	167.1	16.3	2623
Co	114.8	12.9	248.9	28.0	1768
Ni	111.9	12.6	266.1	29.9	1728
Cu	105.1	11.7	276.1	30.8	1358
Al	57.8	21.4	181.8	67.3	934
Nb	60.2	12.6	127.3	14.9	2750
Sn	43.6	5.97	86.9	11.9	505
Ta	70.0	4.2	138.0	8.3	3290
Au	87.2	4.5	194.0	10.0	1337
Pb	39.2	3.4	79.4	7.0	600

Table 3: Ionization energies and melting points of various metals [33]

Metal	Fractional Ionization (%)	
	Near Threshold Fluence	At 10 Times the Threshold Fluence
Al	21.7	52
Ni	2.9	20
Nb	8.8	-
Sn	24.7	-
Ta	4.7	20
Au	10.3	32
Pb	40	-

Table 4: Fractional ionization of various metals near the threshold fluence and at 10 times the threshold fluence [35]

the combined amount consumed to vaporize and ionize Cu. Based on this analysis, it appears that the minimum ablation energy calculated previously accounts for only a small portion of the actual energy required when performing PLA. Furthermore, because of factors such as fractional

ionization, ionization energy and absorption efficiency (determining KE of ions), the ratio of minimum ablation energy between two metals, will not be indicative of the ratio of ablation yield.

Another factor influencing the ablation yield is the surface roughness of the target. An initially smooth target surface becomes rough after being illuminated by several laser pulses, which reduces the amount of material ablated by 30-50% [28]. To maintain consistency, a specific part of the target surface can first be ablated to reach a steady level of roughness before performing PLA to synthesize a sample.

The deposition rate is the increase in the thickness of the metal film after each laser pulse. While it is highly dependent on factors that are specific to each laser setup, the work by Svendsen et al. [36] provides a general estimate of what can be expected. They found that the thickness deposited on the substrate per pulse using a Ni target is on the scale of 0.001 nm or "a few percent of a monolayer." This underpins the suitability of PLA for bimetallic NP catalyst synthesis, since the deposition of an entire monolayer will cause the NPs to become connected to adjacent NPs, reducing the surface area and catalyst activity. Their measured deposition rate as a function of fluence is shown in Figure 11 [36]. It was also found that the use of a 532 nm wavelength laser results in a higher deposition rate compared to the 355 nm laser with the same fluence. This agrees with the results from Torrisi et al. [34].

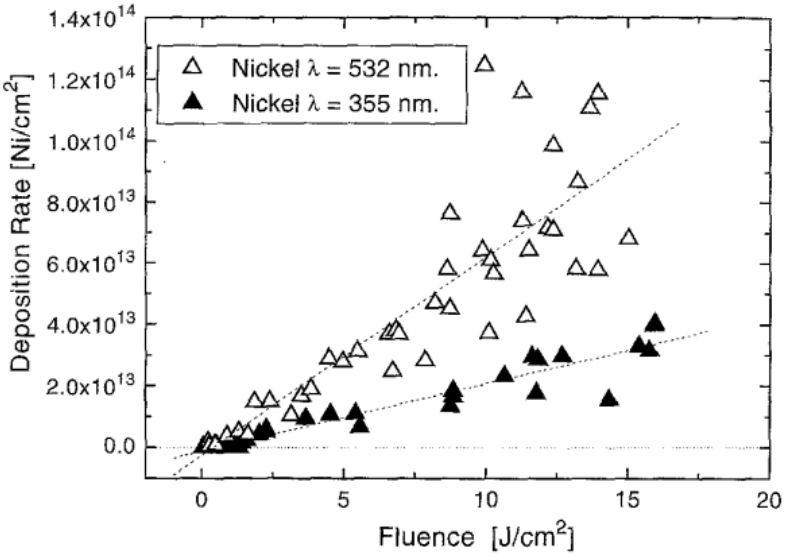

Figure 11: Deposition rate of nickel with 532 and 355 nm lasers as a function of fluence [36]

The angle of ablation also plays a large role in the deposition rate. In a study by Toftman et al. [37], it was found that the most material is deposited when the beam is perpendicular to the surface as shown in Figure 12. In addition, it was found that an elliptical laser spot with a high aspect ratio results in a higher deposition rate than a circular spot. Another important parameter is the background gas and its pressure. Because a sizable portion of the plume consists of highly reactive ions, an inert background gas is used when the deposition of pure metals is desired. In other cases, a reaction with the background gas may be beneficial. For example, it may be possible to synthesize a CoMoN catalyst in the presence of N_2.

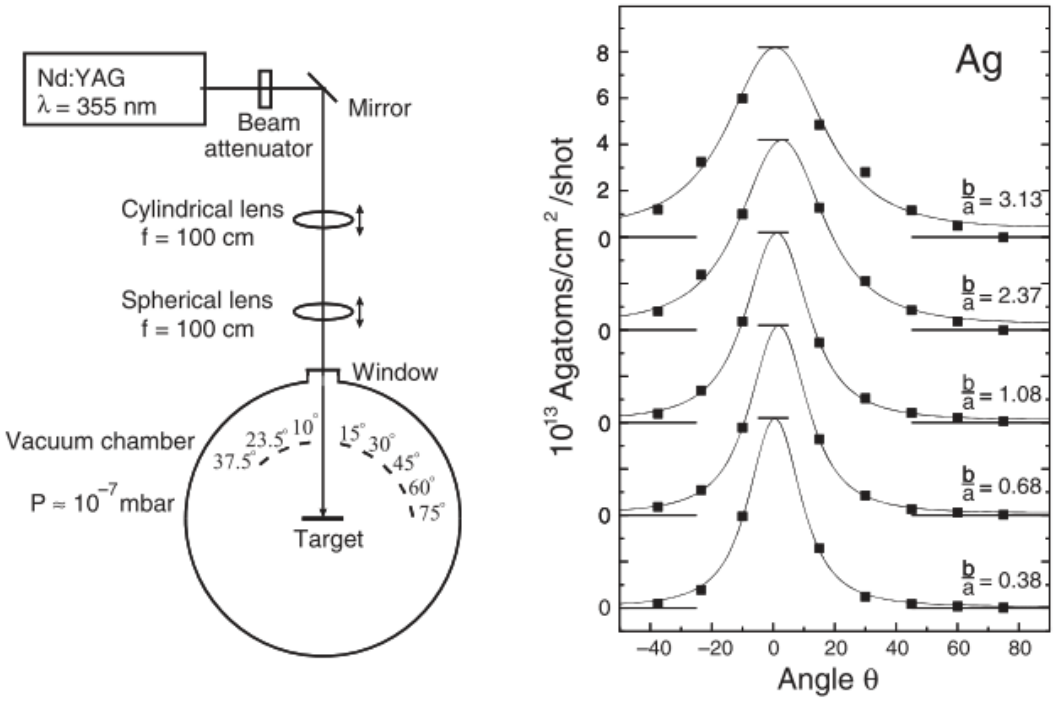

Figure 12: Experimental setup and results from study by Toftman et al. [37]. Shows the effect of the angle of ablation and aspect ratio (for an elliptical laser spot) on the deposition rate.

The issues mentioned in the previous section related to the sonochemical method do not apply to PLA since each pulse only immobilizes a tiny fraction of the required NPs allowing the user to control the amount deposited by varying the number of pulses. Since this is a physical deposition method, no solvents are required. In addition, the high temperatures involved cause the NPs to form stronger bonds with the substrate compared to methods involving solvents; resulting

in less sintering and improved stability [38]. Using this method, McArthur et al. [6] were able to deposit NPs with small diameters and small size distributions on carbon nanotubes. While the problem of the deposition of micron-sized particles was not encountered in this study, Irissou et al. [27] suggested that this would be a major drawback of PLA. The mechanisms causing this include: "subsurface boiling, exfoliation, expulsion of the liquid layer by shock wave recoil pressure, and condensation from vapor species due to supersaturation." It was suggested that adjusting parameters such as the laser wavelength and pulse energy can reduce the number of micron-sized particles. Another recommendation was to use a shutter as larger particles have a much longer flight time. However, since this study uses an experimental setup similar to the one used by McArthur et al. [6], it is expected that there will be no need to implement a strategy to reduce the deposition of micron-sized particles.

The decoration of BNNTs with multiple metals can be achieved. This is done by (a) using a solid alloy target [27], (b) alternating between each metal, or (c) simultaneously illuminating two targets by splitting the laser beam. All methods would allow for a shared interface between the two metals. Arnold and Aziz [39] applied the first approach with a SiGe target and reported that the catalyst's composition diverged from the alloy target. A study by Krebs and Bremert [40] involving 30 different alloys however found that the stoichiometry remained very similar to the target and is minimally affected by laser fluence. Compared to the second approach, the advantage of using an alloy target is that it is possible to control the stoichiometry with a relatively high level of accuracy (for most metal combinations) without requiring the use of characterization methods such as EDX to experimentally determine the relative ablation rate of each individual metal target. The main issue is that a separate target must be obtained for each metal combination and ratio of metals; a problem that will undoubtedly limit the variety of possible catalysts as not all combinations and ratios are offered by vendors. The advantage of the first two options is that the full laser power can be applied, as opposed to the case where a beam splitter would be used to halve the power when simultaneously ablating both materials, which may cause the fluence to drop below the ablation threshold. The number of laser shots applied to each target is controlled in (b) by switching between targets and in (c) by using a shutter to prevent the beam from reaching a target for a certain percentage of pulses. Simultaneously ablating each metal allows the plumes to interact, which may lead to differences in morphology.

Not many studies comparing the morphologies created when using these setups were found for the direct PLA configuration, however Irissou et al. [27] found that for the cross-beam PLA setup with diaphragm as shown in Figure 13, with He used as the background gas, there was mixing at lower pressures whereas between 1.2 and 2.4 Torr (160 and 320 Pa), there was a clear separation between the plumes indicating a reduced level of interaction. The film was found to be more uniform at higher pressures, which is thought to have occurred because weaker interactions resulted in the particles' initial off-axis trajectory being only slightly affected. The pressure was found to be a determining factor of the relative concentration of each metal deposited because the velocity of a heavier atom decreases less with increasing pressure. Therefore, in a Pt-Ru system, Pt to Ru ratio increased with increasing pressure. Finally, the deposition rate was lowest in vacuum and peaked at 2 Torr (267 Pa). On the other hand, McArthur et al. [6] were successful in decorating effective catalysts at 2.5 – 3 mTorr (0.3 – 0.4 Pa).

The deposition rate would only be of interest when considering the scalability of this process. In determining an optimal background pressure in preliminary studies, factors affecting performance such as thermal stability and agglomeration should first be investigated.

McArthur et al. [6] found that activity increases with increasing PLA time and peaks at 40 min before rapidly dropping off. A higher PLA time corresponds to more NPs deposited, which increases the surface area at lower loadings. After reaching a certain threshold, additional particles begin depositing on top of other NPs, resulting in agglomeration and a decrease in surface area, and hence activity.

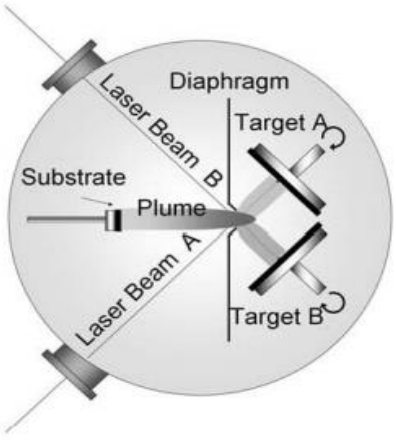

Figure 13: A schematic of the cross-beam PLA setup with a diaphragm [27]

Bimetallic Catalysts

Recall from the 'volcano curve' in Figure 4 that a CoMo catalyst had a higher activity than any other single metal option. While the exact mechanism is disputed, a simplified model suggests that nitrogen binds too strongly to the Mo, allowing easy dissociation of N_2 but limited desorption. The inverse is true for Co. The rationale is that combining these two metals would yield a catalyst closer to the peak [5]. Figure 14 [5] shows that a CoMo-based catalyst provided a much higher turnover frequency with nitrogen vacancies further improving its catalytic properties. It was noted that the enhanced properties only apply when the metals are in close proximity; where many mixed-metal sites are present, which can be achieved through the use of dual-metal nanoparticles. It is believed that even greater values can be achieved by optimizing the Co to Mo ratio.

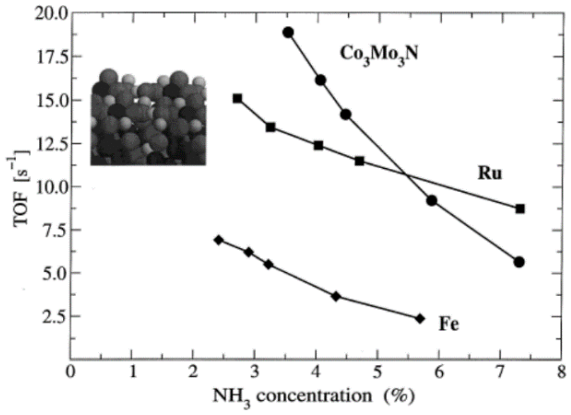

Figure 14: Turnover frequencies plotted against NH_3 concentration for a catalyst with a surface structure of Co_3Mo_3N, a promoted Ru catalyst and an Fe catalyst [5].

Following this logic, it seems that other combinations such as FeRu and MoRu (osmium is avoided due to its high toxicity), combinations of metals on opposite sides of the peak, may also exhibit high activity. In a recent study by Rai et al. [41] FeCo NP catalysts of varying ratios were synthesized using a carbon-nitrogen matrix as the support. Due to their preparation involving wet chemistry, the iron and cobalt were mixed with phthalocyanine to create FePc and CoPc. At 400°C and 7 MPa, the surface of 80% FePc and 20% CoPc was found to yield the highest activity; outperforming an FePc catalyst by approximately 40%. While this result somewhat differs from what can be obtained with plasma-catalytic ammonia synthesis (since temperature is used to provide the activation energy in their work), their analysis of the underlying phenomena explaining

how the addition of Co to an Fe catalyst makes it more conductive to N_2 activation will likely also apply to plasma reactors.

It was discovered that Ni can more easily be reduced when combined with a noble metal [20]. This may be associated with the shifting of Ni further left on the 'volcano curve' in a combination such as PtNi. It is believed that due to many unknown factors such as quantum effects at the nanoscale, in general it will be difficult to predict the synergistic effects between the two metals. The two metals can mix to form alloys or form separate NPs that are in contact with each other [20]. Most research has been done on alloys [20] so there is an opportunity to discover the effectiveness of separate NPs.

Objectives

The overall objective is to successfully synthesize and characterize dual-metal NP catalysts on BNNT supports. The following is a list of deliverables:

- Implementing a mechanism to rotate the substrate at a specified velocity.
- Modification of target holder and incorporation of precise motors allowing an even distribution of ablation across each target surface along an axis and to allow switching between two target metals between laser pulses.
- Developing a computer interface to coordinate the timing of each laser pulse with the rotation of the substrate and displacement of the target holder.
- Depositing NiRu, CoMo and FeRu combinations onto filter paper and determining the deposition rate using ICP-AES.
- Performing deposition experiments on BNNT buckypapers and optimizing for finely dispersed bimetallic NP coatings.
- Characterizing the morphology, composition and chemical states of the coatings using a scanning electron microscope (SEM) and an x-ray photoelectron spectrometer (XPS) before and after exposure to heat, plasma and simultaneous application of both.

Experimental Considerations

Laser Setup

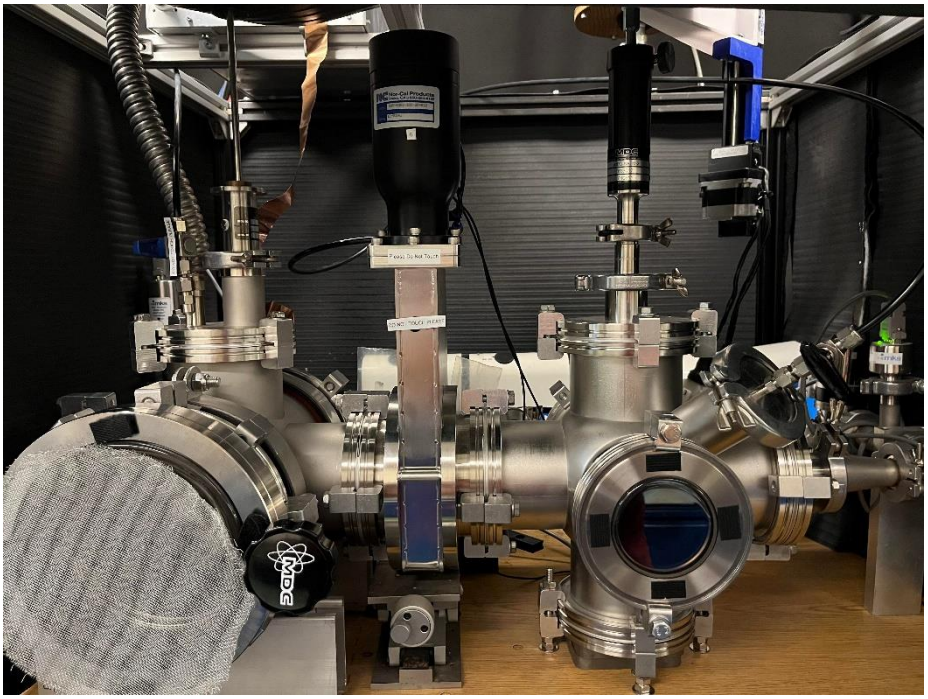

Figure 15: PLA setup.

The experiment involves placing metal targets and substrates inside a vacuum chamber in the arrangement as shown in Figure 15; a similar layout to the one presented by Irissou et al. [27], as shown in Figure 13, with the incident laser beam illuminating the target at 45˚. The chamber can reach pressures as low as 10^{-6} Torr (1.33×10^{-3} Pa) with the background gas only consisting of argon. This is done by first lowering the pressure to ~0.1 Torr (13.3 Pa) using an Alcatel Adixen 2005SD Dual Rotary Vane Vacuum Pump before opening a valve to connect an Adixen Pfeiffer MDP-5011 Turbo Drag High Vacuum Pump. A Brilliant Nd:YAG laser with a wavelength of 355 nm (third harmonic), maximum energy per pulse of 185 mJ, repetition rate of 10 Hz, pulse length of 4-6 ns, and beam divergence of 0.5-0.7 mrad is used to perform PLA. The exact value of the beam divergence is not known but is based on the repetition rate according to the user manual [42]. The laser is focused at the target using a lens, creating a plume, which deposits the metals onto the substrate. The metals are sequentially ablated; the laser is directed at one metal for a specified

number of pulses before ablating the other material. To estimate the fluence, the following equation for a Gaussian beam is applied [43]:

$$tan\theta_0 = \frac{\lambda}{\pi\omega_0}$$

where θ_0 is the half angle and is thus between 0.25 and 0.35 mrad, λ is the wavelength and ω_0 is the beam waist which is defined as the narrowest radius of the beam (found when it is perfectly focused). Figure 16 [43] shows a diagram of the cross-section of the beam. The beam waist is therefore 0.32 – 0.45 mm and thus the spot size is 0.33 – 0.64 mm^2 for a circular beam. Using this value, the theoretical fluence is 28.8 – 54.5 J/cm^2. It is expected that the actual value would be much lower as the setup involves illuminating the target at 45˚, which is found to ablate less material than at 0˚ [37]. Additionally, the beam is aligned manually by rotating mirrors, causing the focus to not exactly be at the surface of the target which would slightly increase the spot size. Other factors such as the reflectance of the mirrors and lens, and the age of the laser system (~10 years) may lead to decreased fluence as well.

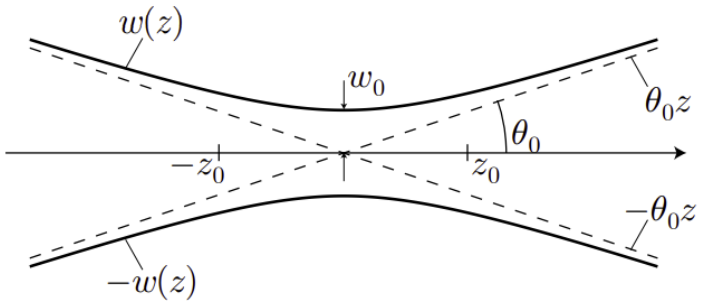

Figure 16: Diagram of a Gaussian beam centered at the beam waist [43].

Substrate Rotation

The substrate is mounted onto a shaft to remain in place inside the vacuum chamber. A spur gear has been added to the end of this shaft to allow rotation using a Sparkfun ROB-13656 bipolar stepper motor. This motor provides a maximum torque of 125 oz. in (0.88 N-m) and has a resolution of 200 steps/revolution. The motor is driven using a DFRobot TB6600 Stepper Motor Driver, which is controlled by an Arduino. By rotating the substrate, it can be ensured that uniform deposition occurs at every polar angle. The stepper motor has been mounted using a cylindrical pin as shown in Figure 17 to allow the user to engage/disengage the gears by tilting the motor towards/away from the shaft. Initially, the entire system except the stepper motor was 3D printed with PLA (polylactic acid) filament. It was found that the gears did not mesh properly so metal gears were used instead. Since the shaft connects to the inside of the vacuum chamber, it is important to minimize vibrations as an excessive amount will temporarily break the seal and cause the pressure to increase. Initially, the stepper motor was set to immediately reach its maximum speed but was modified to instead accelerate to the desired speed, greatly reducing the vibrations produced.

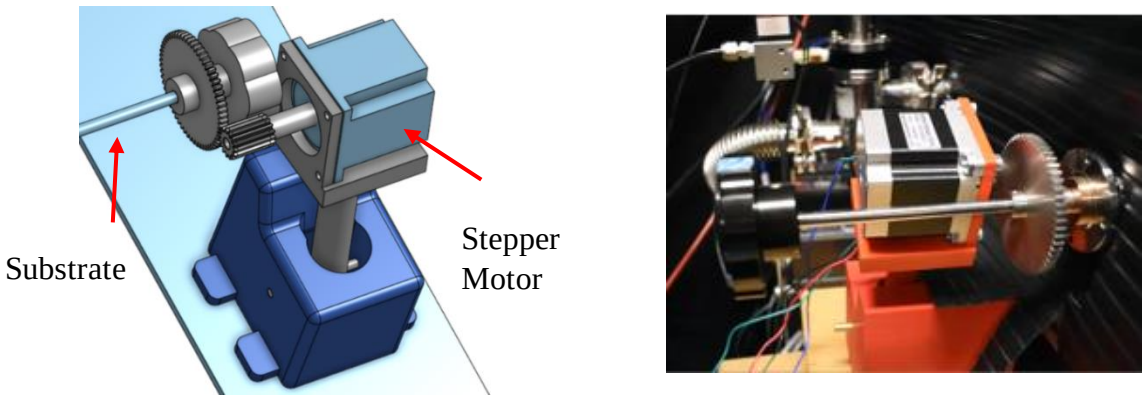

Figure 17: A schematic of the of the substrate rotation system (left) and its implementation (right).

Target Holder

Figure 18 shows a model of the target holder design. There are two 1" holes for each metal target, which are mounted from behind (the side of the holder facing the opposite direction of the laser). The rod attaches to the linear feedthrough at one of the smaller holes. Since the substrate holder is placed inside of a vacuum chamber, it will be machined and made using 304 stainless steel. The holes are off-center because the laser is aligned several mm to the side of the pin onto which the target holder is mounted.

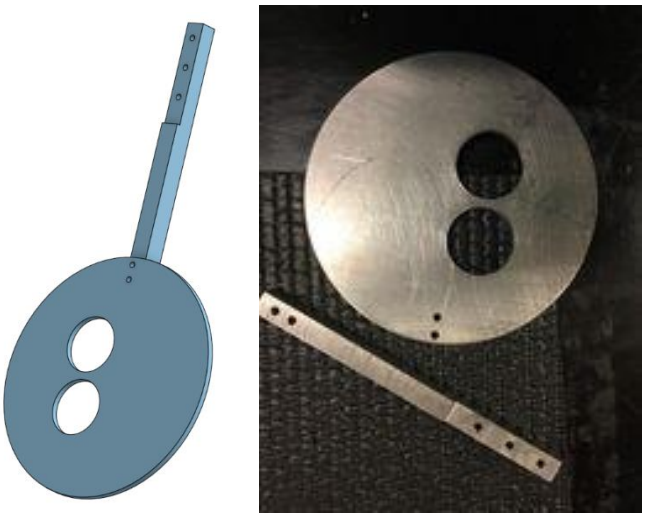

Figure 18: A 3D model of the target holder (left) and a picture of the holder (right)

Target Translation

Since the laser is directed at a fixed spot, to ablate both metals it is necessary to move the target holder vertically. A MDC Precision push-pull linear feedthrough with 2" travel (Figure 19 [44] is used to transmit the motion provided by the VELMEX XSlide™ linear displacement stage (shown in Figure 20 [45]), which is secured to the top crossbar of the laser setup, to the vacuum chamber as shown in Figure 21. This allows sequential ablation as well as the distributing of target erosion across a larger proportion of the target.

Figure 19: MDC Precision push-pull linear feedthrough with 2” travel [44]

Figure 20: VELMEX XSlide™ linear displacement Stage [45]

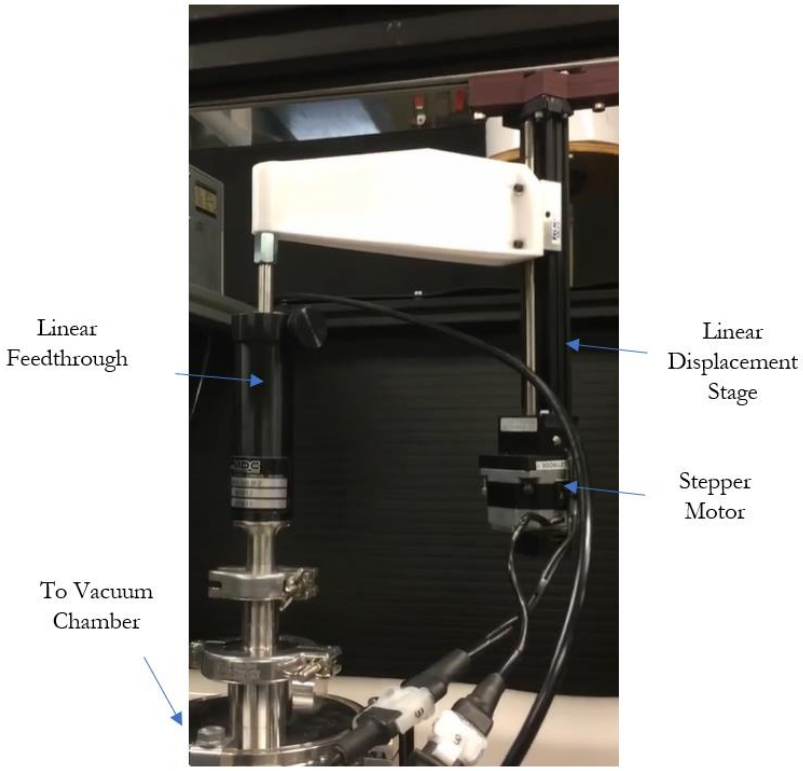

Figure 21. Setup used for vertically translating the target holder. The stepper motor rotates the lead screw which raises and lowers the stage, which is connected to the linear feedthrough with a rigid interface.

Automation Overview

A LabVIEW™ program is used to control the substrate rotation speed, the movement of the target holder, and the laser operation. This allows precise coordination between these systems and permits the flexibility to adjust the operation as various parameters such as target geometry, and desired nanomaterial composition are varied. Figure 22 shows the user interface. The flashlamp delay, which controls the energy delivered per laser pulse can also be adjusted but is always set to 215 μs to deliver the maximum amount.

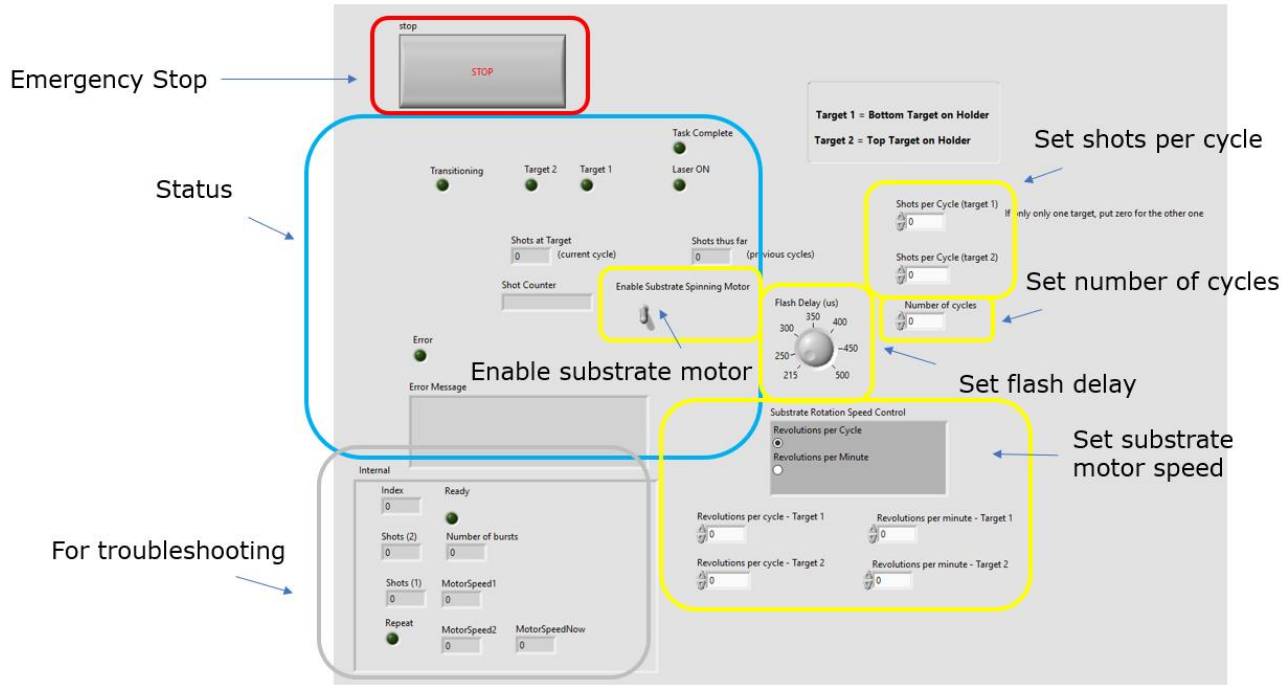

Figure 22: LabVIEW™ user interface for setting the desired parameters of the PLA system.

Substrate rotation is accomplished via a USB serial connection between the computer and an Arduino, which controls the stepper motor driver. The user interface allows for adjustment of the rotation speed. A VXM Stepping Motor Controller is used to set the rotation speed of the stepper motor used for target displacement. Since the change in angle of the stepper motor is determined by the number of pulses sent, the position of the stage is known and thus the vertical displacement of the target holder can be set to alternate between two fixed positions. It is important that this position is fixed in order to maintain consistency, as it was found previously in literature that the target ablates the fastest on a fresh site and gradually slows due to surface roughness until reaching a steady rate. The stepper motor is hardcoded to rotate at the maximum speed without

stalling. The RS-232 communication protocol is used to interface with LabVIEW™. The RS-232 communication protocol is used to interface the laser with the computer. Parameters such as laser modes, pulse energy and frequency can be controlled.

LabVIEW™ Programming

LabVIEW™ is a visual programming environment designed by National Instruments that offers similar functionality to conventional programming languages such as Python and C++. Unlike these languages whose programs consist of lines of code, a LabVIEW™ program is represented as a block diagram. *Blocks*, which act as functions, are connected with *arrows*. In this way, packets of information known as variables, flow according to the program's design. For example, addition can be performed by passing two variables into the "+" block as shown in Figure 23. Various instruments can be controlled using built-in VISA functions. After instantiating the device, it is represented as a VISA-type variable. Similar to how arithmetic is performed, this variable flows through arrows and is passed sequentially into blocks, which represent commands; the most common of which being read and write.

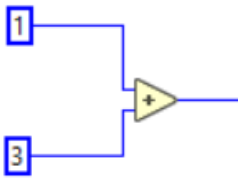

Figure 23: A basic block diagram showing how addition is performed in LabVIEW™.

A *while loop* is a structure that repeats itself until a specific end condition is satisfied. Figure 24 shows an example of a while loop used to iterate five times. The loop exits when a Boolean with a true value is passed into the red circle. The *equal* block only outputs a true Boolean when the output of the *sum* block is five. As will be seen later, this structure is used extensively in this program.

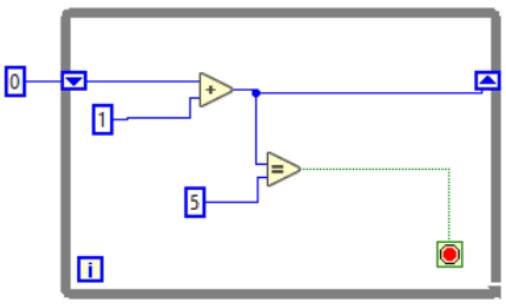

Figure 24: An example of a while loop that iterates five times.

It is important to note that while programming languages execute each line of code sequentially by default, LabVIEW™ automatically processes all functions in parallel; with the caveat being that a function can only begin once it receives all of its inputs. Thus, processes can be synchronized by using a block like the one shown in Figure 25, which ensures that processes 3 and 4 will begin at the same time. Without this timing block, process 4 will begin before process 3 since process 2 (on which process 4 is dependent) finishes before process 1. My program uses this technique since each instrument takes a variable amount of time to perform internal functions but must be synchronized with each other.

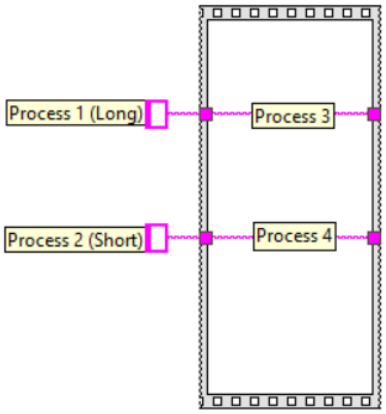

Figure 25: A single timing block used to ensure that process 3 and process 4 begin simultaneously.

This program completes several tasks, each of which comprising of multiple functions. In this section, the tasks will be described in chronological order from the time the user starts the program. Before the other modules execute, each variable that is visible on the front panel is initialized. This ensures that no old values remain from prior operation. The laser, the Arduino and the linear displacement stepper motor controller are connected in parallel using the aforementioned VISA functions. Commands are sent to the laser before, during and after firing. The initial commands consist of the repetition rate (number of shots fired per second), the flash delay (responsible for the intensity) and flashlamp voltage among others. With command "QSM1", the laser is set to operate in *burst mode*, which allows the program to specify the number of shots. This is the safest option since the laser will stop shooting once the command is finished even if communication with the computer is severed. Each command comprises of upper-case ASCII strings that must end in carriage return and line feed characters. For more details, refer to the laser manual [42]. Since the communication between the laser and computer is inconsistent, causing

incorrect data to be received by the computer, a while loop is employed when reading data which iterates until the expected information is received. Another while loop is used to make sure that reading doesn't commence before any data has arrived. Since these sequences are performed every time a command is sent to the laser, a *subVI* is used for communicating with the laser as shown in Figure 26. A subVI, which is analogous to a function in programming languages, is a user-defined block that incorporates multiple sub-blocks with the goal of eliminating the need to duplicate code and reducing clutter. The algorithm show in Figure 26. is seen as a single block in the block diagram, with an output being the laser's answer to the command as a string.

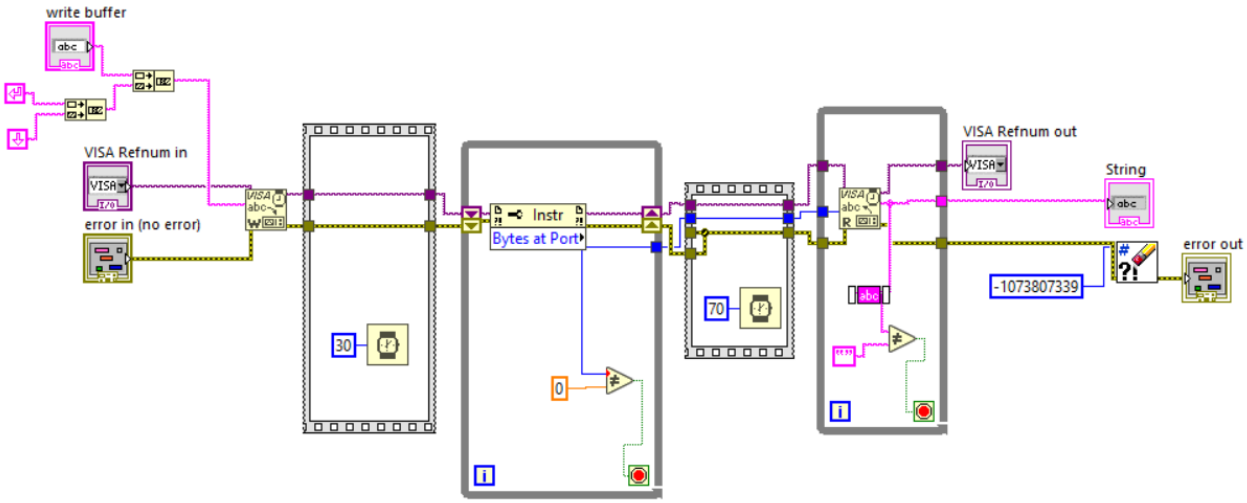

Figure 26: The subVI used to communicate with the laser. Receives a string command and outputs the VISA variable and laser response.

The TB6600 stepper motor controller rotates the stepper motor by a set fraction (specified by switches on the side of the device) of one revolution every time it receives a pulse from the Arduino. Thus, in order to set the correct stepper motor speed for substrate rotation, the delay between each pulse sent by the Arduino must be calculated. Once communication with the Arduino is established, the stepper motor is turned on using this delay. The stepper motor continues spinning until a command to change its speed is received or the program terminates.

Similar to the laser, communication with the VXM Stepping Motor Controller for the vertical displacement of the targets involves specific commands, which can be found in the user manual [45]. The stepper motor rotates a screw which changes the position of a slide block in one axis. When turned on, the controller does not know the position of the slide block. It can be oriented

by moving the stage to either its maximum or minimum displacement where pushbuttons can be found; a functionality that is implemented in the LabVIEW™ program. The motor is then set to move the slide block to the position where the first target to be ablated is aligned with the laser. A command is sent to slowly oscillate the position of the target to prevent excessive ablation at a single point. When orienting itself or moving between two targets, the stepper motor is set to accelerate to the maximum speed possible without stalling.

With the devices ready, it is now time to fire the laser. The flashlamp is turned on and the main laser control logic, shown in Figure 27 is executed. The algorithm is placed in a two-frame *flat sequence* structure, which ensures that all functions in the left frame are completed before the right frame is run. The left frame consists of a while loop placed in a *case structure*. There are two versions of code that can run in a case structure depending on the value of the input Boolean; making the case structure analogous to *if statements* in programming languages. In this case, the blocks displayed are almost always run, with the exception being when the user presses the stop button.

The "CC" command activates the Q-switch, causing the laser to shoot the previously specified number of shots. The "UFQ" command requests the current number of shots fired. This is included twice as the laser was found to provide an answer to the previous command. Upon each iteration of the while loop, the number of shots fired in this round and in total over the course of the experiment is updated in the front panel. "Shots thus far" refers to the number of shots fired in previous rounds and "Shots at Target" is the number in the current round and is calculated by subtracting the former from the value read from the laser. When the specified number of shots is reached, the loop is exited. The algorithm keeps track of the targets using the "Target 1" and "Target 2" Booleans, which are never simultaneously true. The code in the loop sets either "Shots (1)" or "Shots (2)" as the required number of shots depending on these variables. Even if the connection between the laser and computer is lagging, the laser will not shoot more than the appropriate number of shots.

The right frame sets both "Target 1" and "Target 2" variables to false and "Transitioning" to true. This provides the signal to the vertical displacement algorithm to begin transitioning to the next target. In addition, if the angular velocity of substrate rotation during ablation of each target is different, then the stepper motor used to rotate the substrate is decelerated, stopped, and

accelerated to its new speed. The “CS” command deactivates the Q-switch. When the slide block reaches the next target, “Transitioning” is set to false, providing the signal to the laser algorithm to proceed. The appropriate target variable is set true and all of the logic in Figure 27. executes once again (this is nested in a larger loop not shown in the figure).

The block diagram contains the “Repeat” variable, which is excluded in the above description. This is relevant only when the user requires over 1000 laser shots fired. Since the laser allows an input of up to 999, the algorithm works by inputting this and subtracting it from the actual value. When all cycles are complete the flashlamp is turned off and the Arduino sends a command to cease substrate rotation.

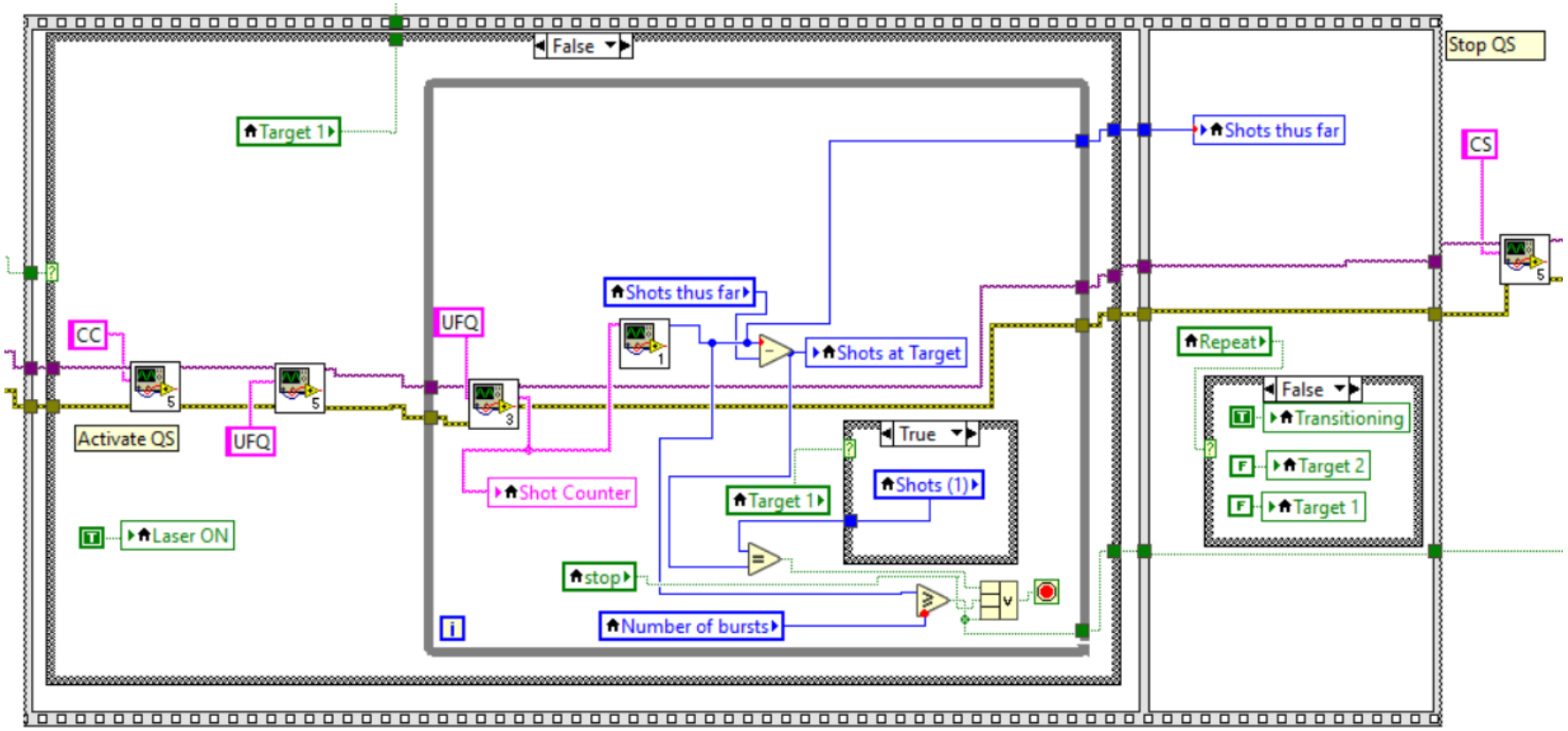

Figure 27: The main logic used to keep track of the number of laser shots. Updates the user interface each time the laser shot counter increments. Exits the loop once the specified number of shots is fired and sends signal to switch to next target.

Thermal / Plasma Reactor

The reactor, shown in Figure 28, allows for heating and/or argon plasma treatment of the substrate, which is mounted on a plate with a diameter of 1.75 in (4.45 cm), in a vacuum. The argon is supplied by Praxair and has a purity of 99.999% (grade 5.0). A Varian DS-302 Rotary Vane Pump is used to reduce the pressure to as low as 1.8 mTorr (0.24 Pa) at room temperature. A Eurotherm® 2416 Temperature Controller (a PID controller), connected to a Blue Wave Substrate Heater Power Supply, raises the temperatures to the setpoint and maintains it. A 13.56 MHz capacitively-coupled RF plasma is generated using an Advanced Energy® RFX600 Generator; with the Advanced Energy® 3155039-003 Tuner Controller as the matching network. The RF electrode is placed directly above the substrate mounting plate, which acts as the ground electrode.

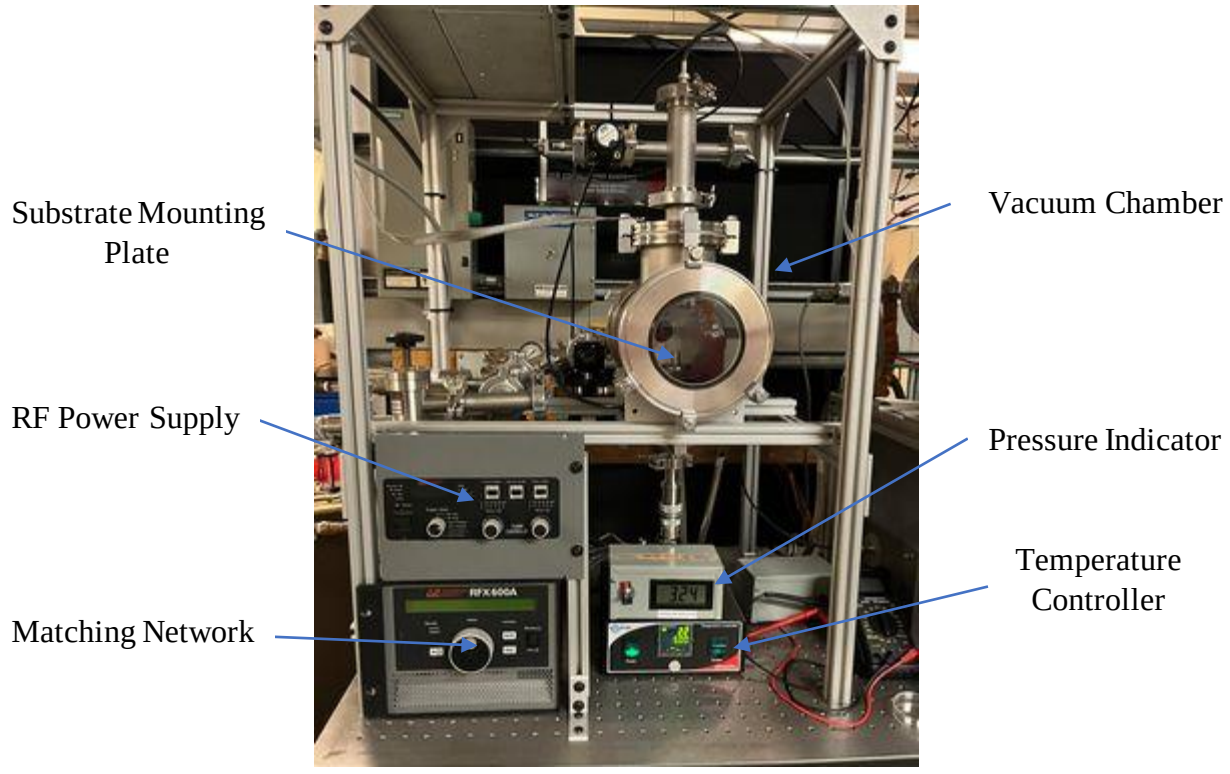

Figure 28: Thermal / plasma reactor setup

Methodology

Preparation of Samples

The first step in producing bimetallic NPs on a BNNT substrate is loading two metallic sputtering targets onto the target holder. The targets are supplied by Kurt. J Lesker Co., with specific details provided in Table 5. BNNT buckypaper, produced by solvent dispersion and vacuum filtration [46] is supplied by the NRC. A buckypaper, which can be characterized as thin, flexible yet brittle, and has an off-white appearance (as shown in Figure 29 [47]) is cut into a 4x4 cm^2 square and loaded onto the substrate holder using clips. The clips are placed as close to the edge of the buckypaper as possible as the surface below them do not get coated. The target and substrate holders are then placed inside the vacuum chamber. Next, the chamber is depressurized. After reaching 1 Torr (133 Pa), argon is purged for 2 -3 min. Despite there being a very small number of gas particles in the chamber at the operating pressure, it is still important to purge argon to ensure that no reactions take place between the gas and metal plumes. Once complete, the pressure is lowered to $\sim 5 \times 10^{-5}$ Torr (6.67 mPa), the pressure at which the samples are synthesized.

The appropriate settings are selected in the LabVIEW™ user interface. In this context, one cycle refers to a set of laser shots towards a target before switching to the next metal. The number of shots per cycle is chosen based on the desired ratio. This value is set low to prevent thick layers of distinct metals from being deposited. The number of cycles refers to the number of times the targets alternate before ending the process. The product of these values is the total number of shots for the given target. The speed of substrate rotation is set to ensure uniform deposition across the surface. Thus, a value was always chosen so that the substrate spun an integer number of full rotations per cycle.

Once the process is complete, the chamber is repressurized and the sample is carefully removed. After discarding the portions covered by the clips, the BNNT buckypaper is cut into multiple smaller samples. This allows for the comparison between samples of the same batch, removing sources of error from variations between different BNNT batches, for example.

Metal	Purity	Part Number	Diameter
Fe	99.9%	EJTFEXX303A1	3” (7.62 cm)
Ru	99.95%	EJTRUXX351A2	1” (2.54 cm)
Co	99.99%	EJTCOXX401A2	1” (2.54 cm)
Mo	99.95%	EJTMOXX35A4	3” (7.62 cm)
Ni	99.995%	EJTNIXX453A1	3” (7.62 cm)

Table 5: Details of each sputtering target.

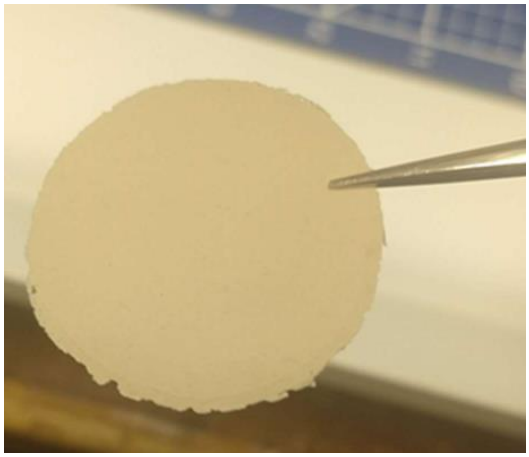

Figure 29: BNNT buckypaper [47]

Stability Testing

The sample is placed on the heating plate in the thermal/RF reactor and held in place with a ceramic washer. For the case of temperature tests, the pressure is lowered to 1.8 mTorr (0.24 Pa) before the temperature controller is set to ramp the temperature to the desired value. Once reached, the sample is left for 15 min before the controller is turned off. After cooling overnight, the reactor is repressurized and the sample is carefully removed. A preliminary study was done in which FeRu and CoMo samples were placed in the reactor at 400 and 500°C. Deformation of the surface morphology was visible for the higher temperature samples, but not for 400°C ones. Thus, the temperature of the samples exposed to both heat and plasma was also set to 500°C, so as to observe more pronounced changes. For the case of the NiRu catalysts, the reduction temperature found

using temperature-programmed reduction (TPR) is applied. This is because it will be necessary to reduce the catalyst before use.

For plasma stability tests, an argon plasma of a maximum power of 9.5W (half of the 19W delivered from the RF power supply given equal distribution of power across the two electrodes) is applied to the samples at 1 Torr (133 Pa) for 15 min. Since the heating plate has a diameter of 1.75 in (4.45 cm), the sample is subjected to a maximum of 1.22 W/cm^2. The actual power density would be less due to radiation and edge effects. Losses due to heating are assumed to be negligible as the samples did not exceed 30˚C from heating by the plasma. A ceramic washer is placed on the edge of the sample to allow most of its surface to be exposed unobstructed; with subsequent SEM and XPS tests analyzing the center of the sample. The combined plasma and thermal stability tests consist of simultaneous exposure to both of the conditions outlined, with the pressure set to 1 Torr (133 Pa) in an argon environment.

Characterization

X-ray Photoelectron Spectroscopy

X-ray photoelectron spectroscopy (XPS) involves applying x-rays to a sample and measuring the kinetic energies (KE) of photons emitted by the surface via the photoelectric effect [48]. The binding energy (BE) is the energy required to eject the photoelectron as shown in this equation [48]:

$$KE = h\upsilon - BE - \phi_s$$

where $h\upsilon$ is the energy of the incident x-ray photon and ϕ_s is the spectrometer work function. Each element has a unique range of binding energies, with a few notable exceptions, with slight differences among various chemical states. This is due to each compound having a different polarizability and chemical potential [48]. Thus, the atomic composition can be estimated by counting the number of electrons of each binding energy.

In this study, the Thermo Scientific™ K-alpha X-ray Photoelectron Spectrometer System is used. Since the BNNT samples have a low conductivity, the flood gun is used for charge

compensation. Each sample is analyzed twice at different points with a spot size of 100μm. A survey scan with a resolution of 1 eV covers the entire spectrum (0 – 1300 eV) and is performed for all samples. Narrow scans for specific regions corresponding to a single element, with a resolution of 0.1 eV, are done for each of the two metals covering the surface and for carbon and oxygen, two elements that are always present. The peaks are fitted using the Thermo Scientific™ Avantage Data System. The aim of this study is to explore the ratio of the atomic compositions of each metal deposited for samples with a coating of moderate thickness; fabricated using 3000 laser shots. The NiRu, FeRu and CoMo catalysts are synthesized with shot ratios of 1:1, 2:1 and 1:2; with the 1:1 samples consisting of 1500 shots of each metal, and the 1:2 and 2:1 samples having 1000 and 2000 shots of each metal. In addition, the composition of samples that were heated, exposed to plasma, and subject to a simultaneous application of both, which will be referred to as heated-plasma samples, are compared to unprocessed ones. A total of 36 samples are analyzed with XPS.

Inductively Coupled Plasma Atomic Emission Spectroscopy

Four samples each of NiRu, FeRu and CoMo with equal amounts of each metal are synthesized on 4x4 cm filter paper; with the number of laser shots being 200, 1000, 3000 and 10000. ICP-AES is used to determine the amount of each element in the samples. As opposed to XPS, which only analyzes the surface, this technique quantifies each element in the entire sample with a much higher accuracy. The main disadvantage with ICP-AES is that it is a destructive characterization technique, which involves the digestion of the specimen in acid.

Scanning Electron Microscopy

Scanning electron microscope (SEM) imaging is used to study the morphology of the samples; namely to assess the surface area of the NP coatings on the BNNT buckyapapers and compare as-prepared samples with ones exposed to heat and plasma. The resolutions range from 10 μm – 100 nm.

Results and Discussion

X-ray Photoelectron Spectroscopy

Avantage's built-in survey analysis function is used to obtain an estimate of each sample's atomic composition. Figure 30 shows the spectrum of the as-prepared 1:1 FeRu sample with iron, oxygen, ruthenium and carbon peaks identified. Figure 31 (left) provides the calculated oxygen atomic percentages in each FeRu sample. For the as-prepared, heated, and plasma-only samples, the value is highest when the most iron is deposited, suggesting that iron is usually more readily oxidized than ruthenium. This does not appear to be the case for the heated-plasma samples, whose oxygen content seems to only be mildly influenced by the ratio between iron and ruthenium.

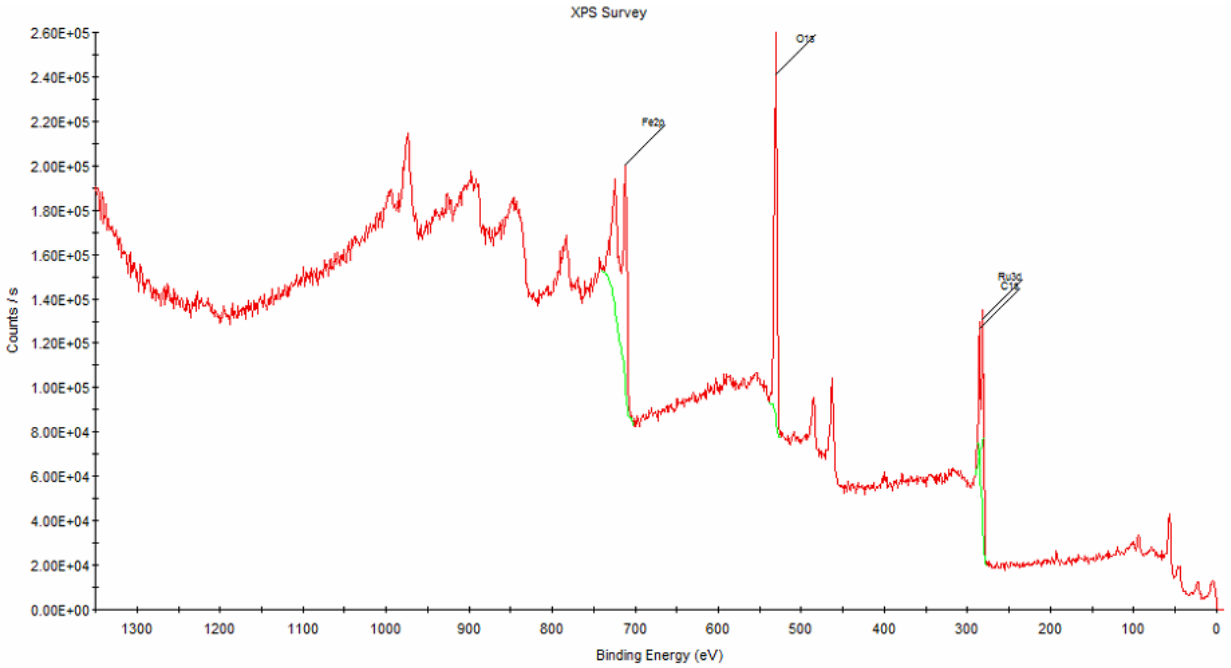

Figure 30: The full XPS spectrum of the as-prepared 1:1 FeRu sample.

The NiRu (Figure 31, right) samples seem to have a fairly consistent amount of oxygen, ranging from approximately 40-50%. The as-prepared sample contains slightly more oxygen than the heated and plasma-treated samples, which have more than the heated-plasma samples. It is important to note that the FeRu samples were heated to 500^{o}C whereas the NiRu samples only reached 415^{o}C; the reduction temperature found using TPR. Therefore, while nickel and iron deposited on BNNTs would respond differently to high temperatures, it cannot be determined

whether FeRu or NiRu samples raised to the same temperature will lose more oxygen. This analysis cannot be done for CoMo samples using the automated survey function since Avantage incorrectly concludes that the cobalt peak is associated with barium, a metal with overlapping peaks that is not found, and calculates an incorrect composition.

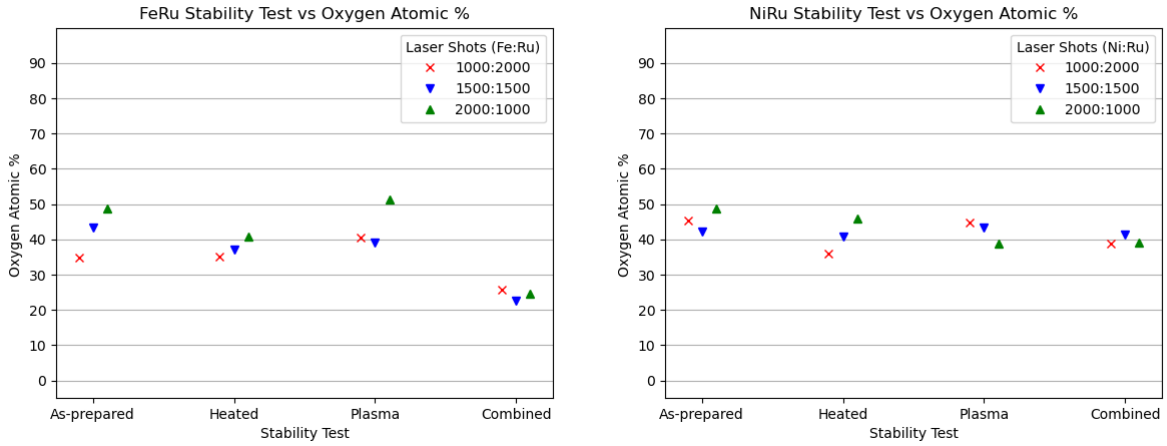

Figure 31: The atomic % of oxygen for each of the shot ratios and stability tests for FeRu (left) and NiRu (right) based analysis of the survey spectra.

Taking the averages of the atomic percentages of iron and ruthenium across all FeRu samples; 1:1, 1:2 and 2:1 Fe:Ru laser shot samples had a Fe:Ru atomic composition ratio of 2.99, 3.33, and 6.05 respectively. While the ratio for the 1:1 sample is approximately half of the one for the 2:1 sample, the 1:2 sample has a higher ratio than the 1:1 sample; an implausible result. This is more likely due to ruthenium and carbon having overlapping peaks, as shown in Figure 32 [49]. Since carbon has a high sensitivity factor (slightly increasing the peak area drastically increases its share of the atomic composition), the values found from this analysis are considered as semi-qualitative and should only be used to compare large datasets to identify trends.

The overlap between the carbon and ruthenium peaks also poses a challenge when manually fitting the FeRu and NiRu peaks. This is because the most prominent carbon peak (C 1s, C-C) peak is always found at 284.8 eV [50] and is commonly used as a reference to correct the spectrum which shifts by variable amount due to charge buildup for insulating samples [51]. In practice, the C 1s peak is set to this value and the other scans are offset by an equal amount. When ruthenium is present, the $Ru3d_{3/2}$ peak eclipses the carbon peak since ruthenium has a much lower sensitivity factor. However, Baer et al. [51] notes that insulators often undergo nonuniform

charging and that using the C 1s peak is unreliable. They recommend using the peak of a known component as an internal reference. For my analysis of FeRu and NiRu, the general position and shape of the Fe2p and Ni2p3 collection of peaks are known and distances between them match only the $3d_{3/2}$ peak of metallic ruthenium; causing it to assume the role of the internal refence. Since the binding energy of the RuO_2 peak is too high, this indicates that metallic ruthenium is the dominant ruthenium species.

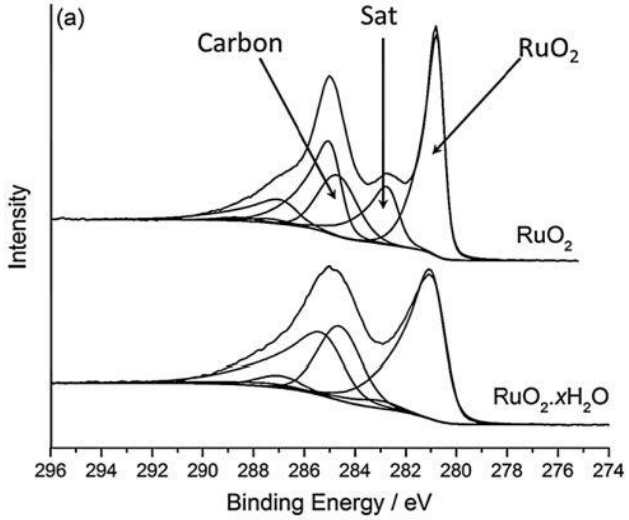

Figure 32: The spectra for anhydrous (top) and hydrated (bottom) RuO_2 [49].

This is an example of a common mistake made when performing XPS analysis. In the *Practical guide for curve fitting in x-ray photoelectron spectroscopy* [52], Major et al. asserts that 30% of papers involving XPS data contain "serious problems," most of which arising from "errors, misconceptions, and bad curve-fitting practices." This is why the *NIST X-ray Photoelectron Spectroscopy Database* which contains data for the binding energies of almost every chemical tested, regularly includes the same peak at multiple conflicting positions. This introduces a level of ambiguity for this study as it aims to discover the chemical state of metals, many of which producing peaks that overlap or are separated by less than 1 eV, by using positions found in literature. Another challenge is that many papers simply show their XPS spectrum with a reasonable fit and state the binding energy of the maximum point, which is inadequate as most metal oxides produce lesser peaks (due to plasmon loss in addition to a fixed proportion of ions temporarily existing in excited states instead of their ground states), resulting in lower kinetic

energies detected and giving rise to shake-up lines at higher binding energies [44, 48], each with unique full-width at half maximum (FWHM) values, which are defined as the distance between the points on opposite sides of the peak at which the height of the Gaussian/Lorentzian curve becomes half of its maximum value; establishing the width of the curve. By carefully evaluating results in literature and including their own findings, Biesinger et al. [49, 50] developed tables containing the peak binding energies, FWHM, and percentage of area for Fe, Co and Ni, and their most common oxides and hydroxides as shown in Table 6. Additionally, data for Ru from a similar analysis by Morgan [49], and Mo from various sources has been included. The data obtained in this study for Fe, Ni and Co are fitted according to the tabulated parameters.

Figure 33 shows an example fit of an iron oxide sample [53]. The sum of each component peak approximates the XPS data. It can be seen that region with a binding energy above ~718 eV is not fitted. The peaks found here occur from multiplet splitting, a phenomenon which occurs when unpaired electrons can reach two final states [52], resulting in a doublet pair. The distance between them is unique for each element, with the separation being 13.1 eV for Fe [52]. The area ratio between the doublets are 1:2, 2:3, and 3:4 for p, d and f subshells respectively [52]. Therefore, when the spectra contains no overlap between the transitions, the doublets on the left side can be ignored. This is the case for Fe, Ni, Co and Ru but not for Mo.

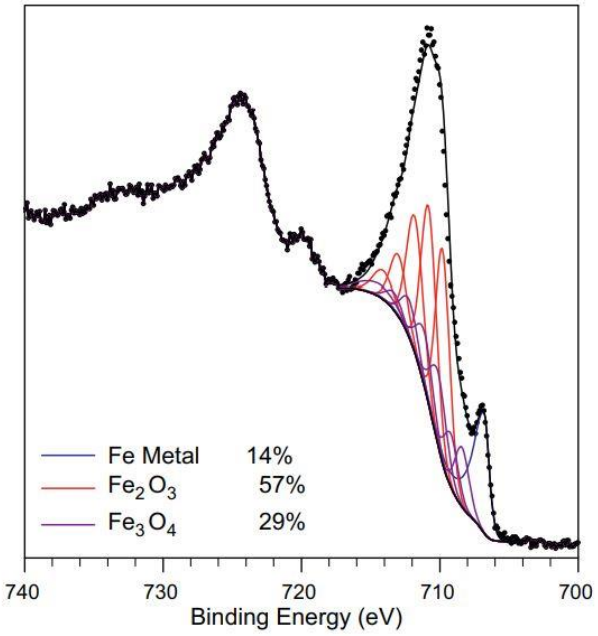

Figure 33: An example fitting of a species containing elemental iron, hematite, and magnetite [53].

Compound	Parameters	Peak 1	Peak 2	Peak 3	Peak 4	Peak 5	Peak 6	Peak 7
Fe	Position (eV)	706.6						
	FWHM (eV)	0.88						
	Area (%)	100						
FeO	Position (eV)	708.4	709.7	710.9	712.1	715.4		
	FWHM (eV)	1.4	1.6	1.6	2.9	2.5		
	Area (%)	24.2	30.1	14.5	25.6	5.6		
Fe_2O_3	Position (eV)	709.8	710.7	711.4	713.3	714.3	719.3	
	FWHM (eV)	1.0	1.2	1.2	1.4	2.2	2.2	
	Area (%)	26.1	22.0	17.4	11.1	14.8	10.0	
FeOOH	Position (eV)	710.3	711.3	712.2	713.3	714.4	719.7	
	FWHM (eV)	1.4	1.3	1.4	1.4	1.8	2.9	
	Area (%)	27.0	26.5	20.6	11.3	6.3	8.3	
Fe_3O_4	Position (eV)	708.4	709.2	710.2	711.2	712.3	713.4	714.5
	FWHM (eV)	1.2	1.2	1.4	1.4	1.4	1.4	3.3
	Area (%)	16.6	14.8	23.7	17.8	12.2	5.7	9.1
Co	Position (eV)	778.1	781.1	783.1				
	FWHM (eV)	0.7	3.0	3.0				
	Area (%)	81.0	11.0	8.0				
CoO	Position (eV)	780.0	782.1	785.5	786.5			
	FWHM (eV)	2.2	2.6	2.4	5.3			
	Area (%)	46.6	25.7	1.6	26.1			
$Co(OH)_2$	Position (eV)	780.4	782.2	786.0	790.4			
	FWHM (eV)	2.0	2.6	4.5	2.3			
	Area (%)	38.1	26.6	33	2.4			
CoOOH	Position (eV)	780.1	781.4	783.1	790.1			
	FWHM (eV)	1.5	1.5	1.5	3.3			

	Area (%)	61.4	24.5	5.2	8.9			
Co_3O_4	Position (eV)	779.6	780.9	782.2	789.5			
	FWHM (eV)	1.4	1.6	1.9	3.2			
	Area (%)	40.5	29.1	15.2	7.2			
$CoMoO_4$ [55]	Position (eV)	781.2	787.4					
	FWHM (eV)	1.4	1.6?0:3					
	Area (%)	60	40					
Ni [54]	Position (eV)	852.7	856.3	858.7				
	FWHM (eV)	1.0	2.7	2.7				
	Area (%)	81.2	6.3	12.5				
NiO [54]	Position (eV)	853.7	855.4	860.9	864.0	866.3		
	FWHM (eV)	1.0	3.2	3.9	2.0	2.6		
	Area (%)	14.3	44.2	34.0	20.7	3.9		
$Ni(OH)_2$ [54]	Position (eV)	854.9	855.7	857.7	860.5	861.5	866.5	
	FWHM (eV)	1.1	2.3	1.6	1.1	4.6	3.1	
	Area (%)	7.4	45.3	3.0	1.4	39.2	3.7	
NiOOH [54]	Position (eV)	845.6	855.3	855.7	856.5	857.8	861.0	864.4
	FWHM (eV)	1.4	1.5	1.4	1.4	1.9	4.0	4.4
	Area (%)	13.8	12.4	9.7	20.7	8.7	23.3	11.4
Ru [49]	Position (eV)	279.8	284.0					
	FWHM (eV)	0.47	0.92					
	Area (%)	60.0	40.0					
RuO_2 Anhydrous [49]	Position (eV)	280.6	284.8					
	FWHM (eV)	0.57	0.91					
	Area (%)	60.0	40.0					
RuO_2 Hydrated [49]	Position (eV)	280.8	285.0					
	FWHM (eV)	1.3	2.1					

	Area (%)	60.0	40.0					
Mo [56]	Position (eV)	227.8	230.85					
	FWHM (eV)	-	-					
	Area (%)	66	33					
MoO_2* [52]	Position (eV)	229.2	232.4	231.2	234.3			
	FWHM (eV)	0.47	0.47	2.23	2.23			
	Area (%)	66	33	66	33			
MoO_3 [52, 53]	Position (eV)	232.65	235.8					
	FWHM (eV)	1.3	1.3					
	Area (%)	66	33					
$CoMoO_4$ [57]	Position (eV)	232.2	235.35					
	FWHM (eV)	-	-					
	Area (%)	66	33					

* Represented by two sets of doublets

Table 6: The position, FWHM and area % for the most common oxides. Data from [53] unless otherwise specified.

It can also be seen that the fitted peaks begin not at zero, but along a curve that stretches only across the region of interest. This curve is known as *background* and is included to account for noise, which becomes more substantial as binding energy is increased, as seen in Figure 30. Figure 33 as well as my analyses make use of a Shirley background. A pattern that is commonly observed when analyzing mixed elemental and oxide specimens is the main elemental metal peak being narrower and at a lower binding energy compared to the oxide peaks. This is evident in Figure 33 with the primary Fe peak being distinctly visible. For some of the samples in this study, this feature is visible and is used as an additional internal reference for charge offsetting. Figure 34 shows the fitted Ni 2p spectrum of a 2:1 heated-plasma NiRu sample. The percentage of nickel found in Ni, NiO, $Ni(OH)_2$, and NiO(OH) are calculated as 20.62%, 22.4%, 6.34% and 50.61% respectively. When compared to the as-prepared sample, shown in Figure 35, the lack of an elemental Ni peak is evident with the nickel states now calculated as 6.38%, 53.96%, 29.5% and 10.16% for Ni, NiO, $Ni(OH)_2$, and NiO(OH) respectively.

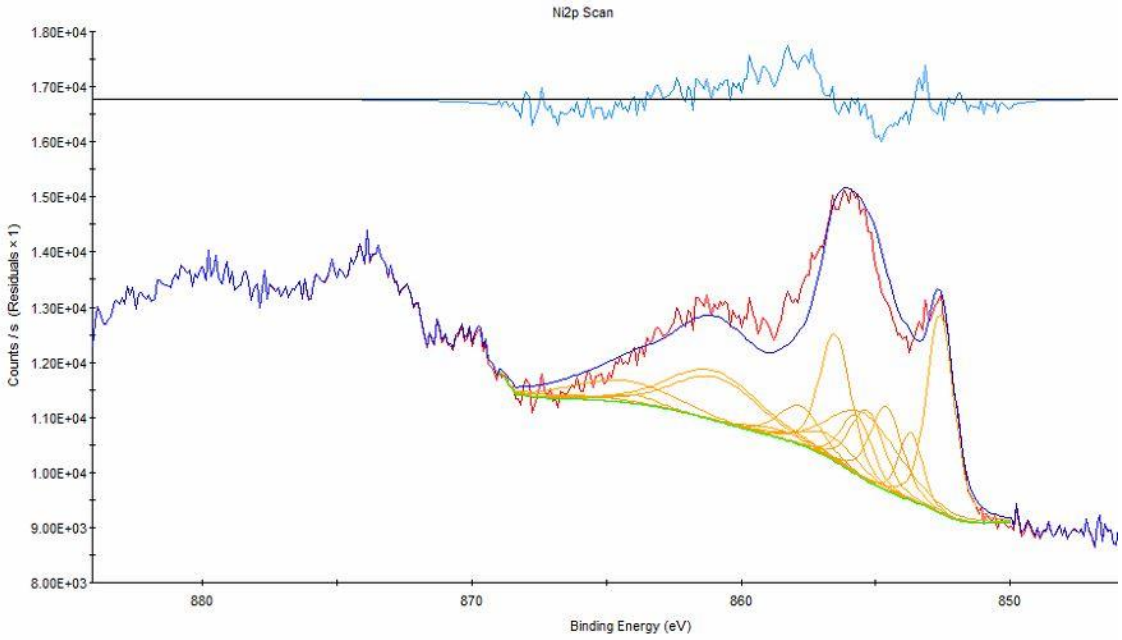

Figure 34: The fitted Ni 2p spectrum of a 2:1 heated-plasma NiRu sample.

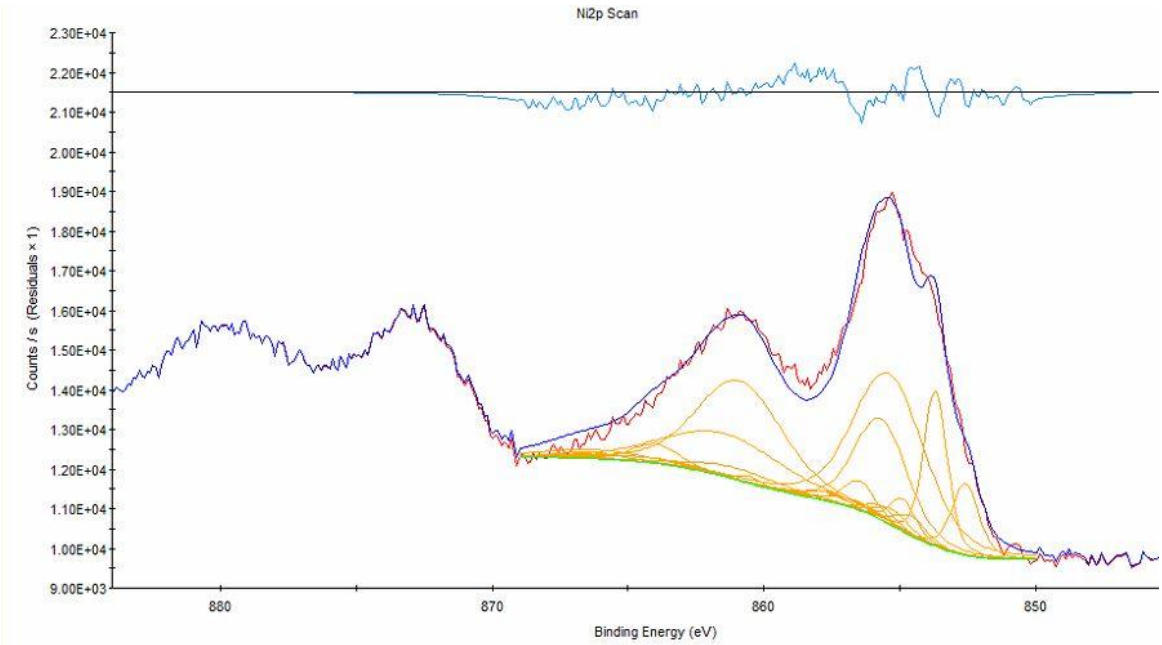

Figure 35: The fitted Ni 2p spectrum of a 2:1 as-prepared NiRu sample.

In many cases, when two points on the same sample were scanned, the percentage of nickel found in the form of Ni and NiO were fairly consistent (not identical due to the heterogeneous nature of the sample) but the $Ni(OH)_2$, and NiO(OH) percentages varied significantly. However, the sum of these hydroxide compounds were consistent, which will thus be used in the following analyses. Figure 36 (left) shows the effect of each stability test on the nickel composition, with the average values across all Ni:Ru ratios reported and the error bars representing the standard devation. The amount of NiO slightly decreases when the specimen is exposed to heat and plasma

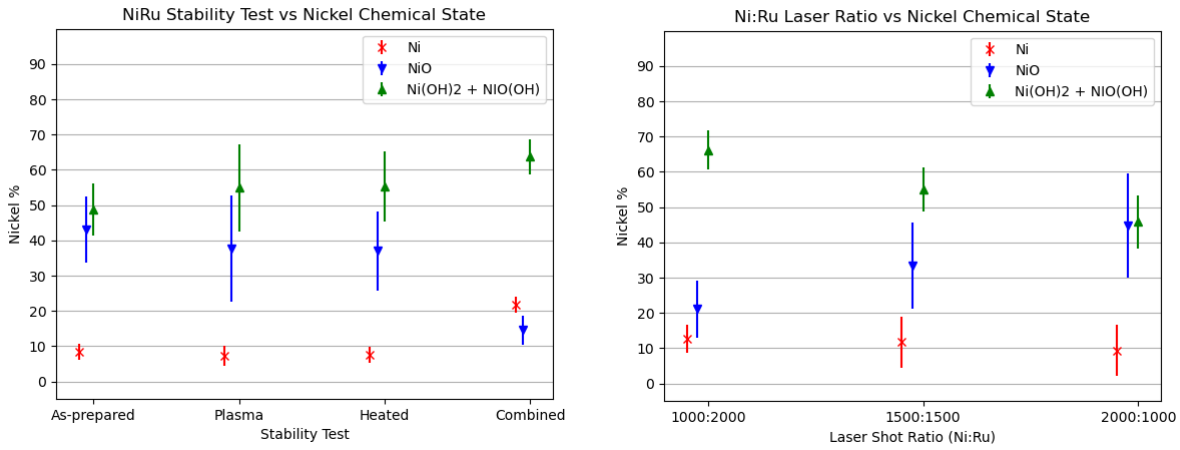

Figure 36: The proportion of nickel found in various chemical states for each stability test (left) and laser shot ratio (right). The error bars represent the standard deviation.

separately. However, concurrent application reduces the amount of NiO to less than half of its original proportion and more than doubles the amount of metallic Ni alongside a roughly 8% increase in the species containing hydroxides. It is likely that the application of heat and plasma causes both the reduction of NiO and a decrease in the surface area, leading to the newly reduced Ni species being unable to oxide when the sample is exposed to air. It appears that the shot ratio between Ni and Ru is another variable influencing the chemical state, leading to more error in Figure 36 (left). This effect can be seen in Figure 36 (right), which indicates that an increase in nickel deposition favors the formation of NiO over hydroxides.

It is not possible to numerically determine the ratio between the ruthenium chemical states since the FWHM of the metallic Ru peak is substantially higher than the expected value as shown in Figure 37. This effect is likely produced by the spectrometer and is handled by fitting Voigt functions instead of Gaussians [52], an operation that is not supported by the available fitting software. Despite this limitation, it can be concluded qualitatively that the ruthenium is mainly in its elemental form since the shape of the spectrum more closely matches that of Ru (Figure 38) than anhydrous and hydrated RuO_2 (Figure 32); with the electron count being low in the region between the peaks.

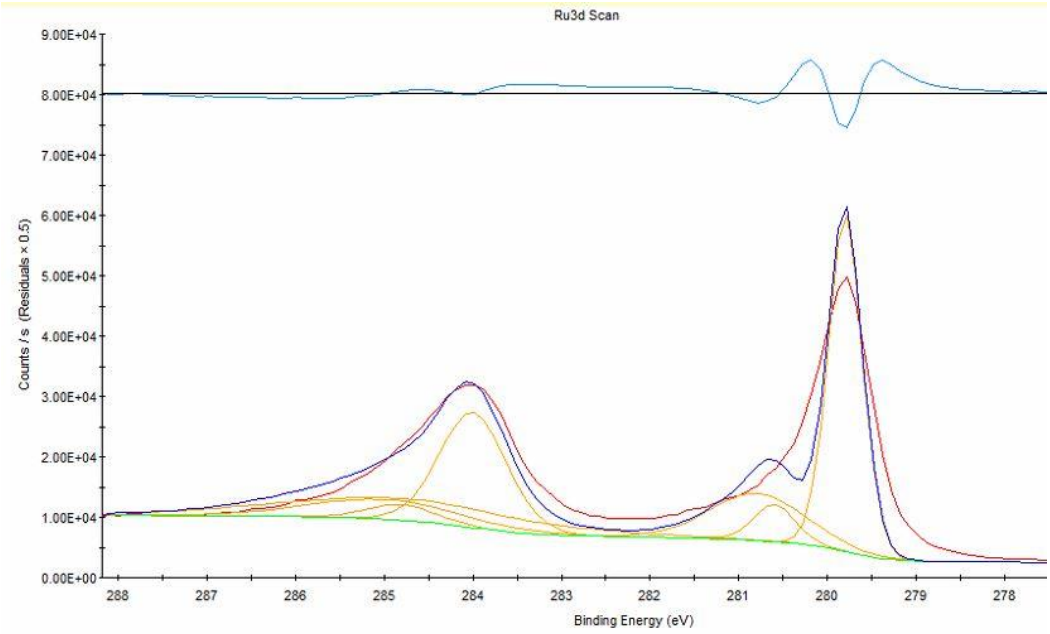

Figure 37: The fitted Ru 3d spectrum showing wider peaks than is expected according to the model.

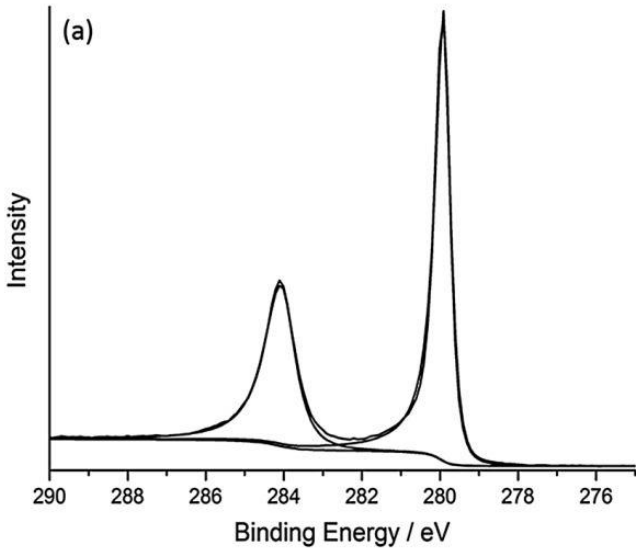

Figure 38: The Ru 3d spectrum for metallic ruthenium [49].

Using the values found in Table 6, an attempt was made to fit the Co 2p spectra of the CoMo samples. However, a portion of the curve consistently did not align with the data, indicating that the model is missing a chemical state. This is why $CoMoO_4$ peaks are introduced. The $CoMoO_4$ spectrum includes a peak at 781.2 eV [57] and a plateau that extends for several eV on the left side of it, as shown in Figure 39. Fitting parameters were not found in literature. Thus, an artificial combination of peaks was developed to model this geometry. With this new addition, it is possible

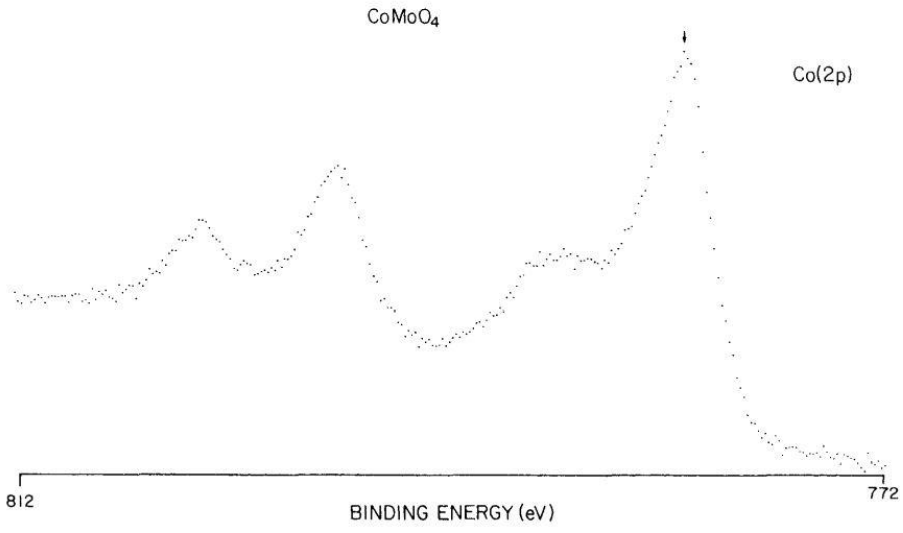

Figure 39: The Co 2p spectrum for $CoMoO_4$ [57]

to reasonably fit the Co 2p spectra of all CoMo samples. Figure 40 shows the fitted data for the heated-plasma 2:1 CoMo sample. Normally, a Shirley background would be used between ~790 eV and 775 eV, which encompasses only the $2p_{3/2}$ region. However, because the $2p_{1/2}$ elemental Co peak overlaps with the $CoMoO_4$ plateau-like structure, it was necessary for the Shirley background to cover the entire binding energy range.

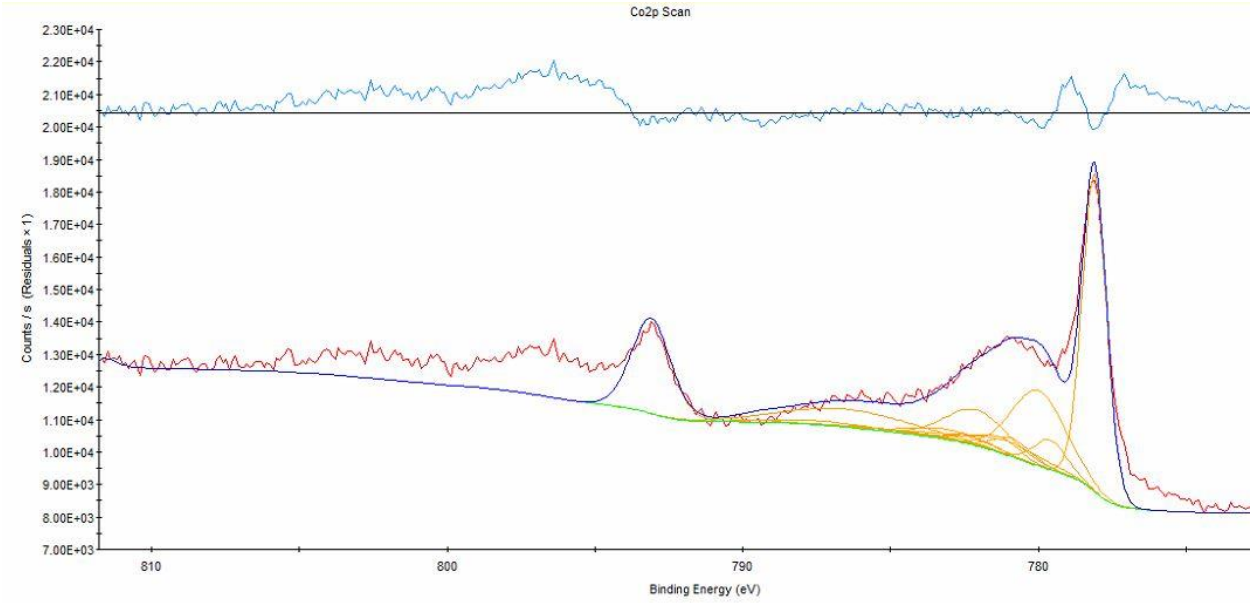

Figure 40: Fitted Co 2p spectrum of a 2:1 heated-plasma CoMo sample.

Figure 41 shows the calculated proportion of cobalt, based on the average across all Co:Mo ratios, in each chemical state. The heat- and plasma-only specimens possess similar compositions, with the most common states being $CoMoO_4$ and CoO, accounting for approximately 40% and 30% of cobalt found, respectively. The as-prepared samples contain more CoO than $CoMoO_4$, with the elemental Co proportion as high as 25%. The most drastic change can be seen in the combined heat and plasma trials, where the amount of $CoMoO_4$ drops to less than 10% and the proportion of elemental Co rising above 40%. Additionally, Co_3O_4 in these samples account for roughly 10%, compared to a negligible (< 0.7%) amount found in all other specimens. This indicates that the CoO is unaffected by the application of heat and plasma, as opposed to $CoMoO_4$ which reduces with the application of both simultaneously. Like in the case for nickel, due to the reduction in surface area, it is likely that most of the newly reduced elemental Co is insulated from the air after removal from the reactor.

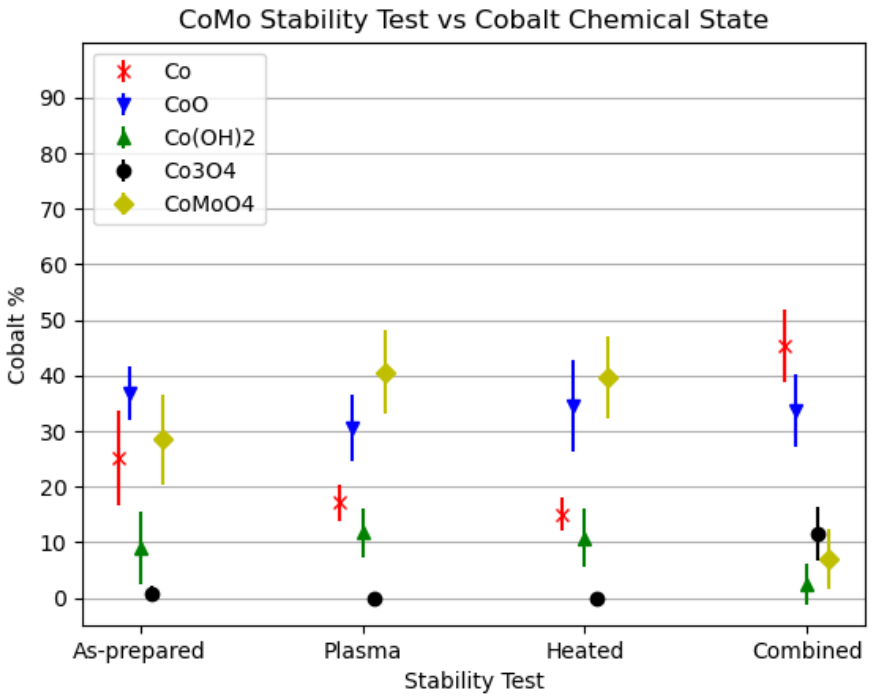

Figure 41: The proportion of cobalt found in various chemical states for each stability test. The error bars represent the standard deviation.

Due to both peak broadening and inconsistent peak positions found in literature, it is not possible to accurately quantify the chemical states for molybdenum. Nonetheless, by comparing the spectra of the specimens of each stability test, as seen in Figure 42, it can be concluded that significant changes to the composition occurs. The peak with the lowest binding energy for every spectra is at 227.8 eV; corresponding to the Mo^0 $3d_{5/2}$ peak. The separation between Mo doublet pairs is 3.15 eV. Thus as expected, the $3d_{3/2}$ peak is found at 230.95 eV. It is believed that the peak between 235 and 236 eV corresponds to the $3d_{3/2}$ peak for $CoMoO_4$, which is found at 235.4 eV [57]. Most likely, this peak is also comprised of the signal from the CoO_3 $3d_{3/2}$ peak, which is found at 235.8 [57]. This can clearly be seen in all every spectrum except for the heated-plasma sample, where a very minor peak is found above 233 eV. This agrees with the Co 2p spectra analysis, which indicates that the amount of $CoMoO_4$ found in the heated-plasma sample is less than a third of what is found in the other specimens. Unlike the other specimens, the signal for the heated sample increases to the left of the Mo^0 $3d_{5/2}$ peak, likely indicating the presence of a relatively large amount of MoO_2, which includes a peak at 229.2 [52]. It appears that the

application of only plasma causes the least change in the chemical state of molybdenum; followed by temperature and a simultaneous application of both.

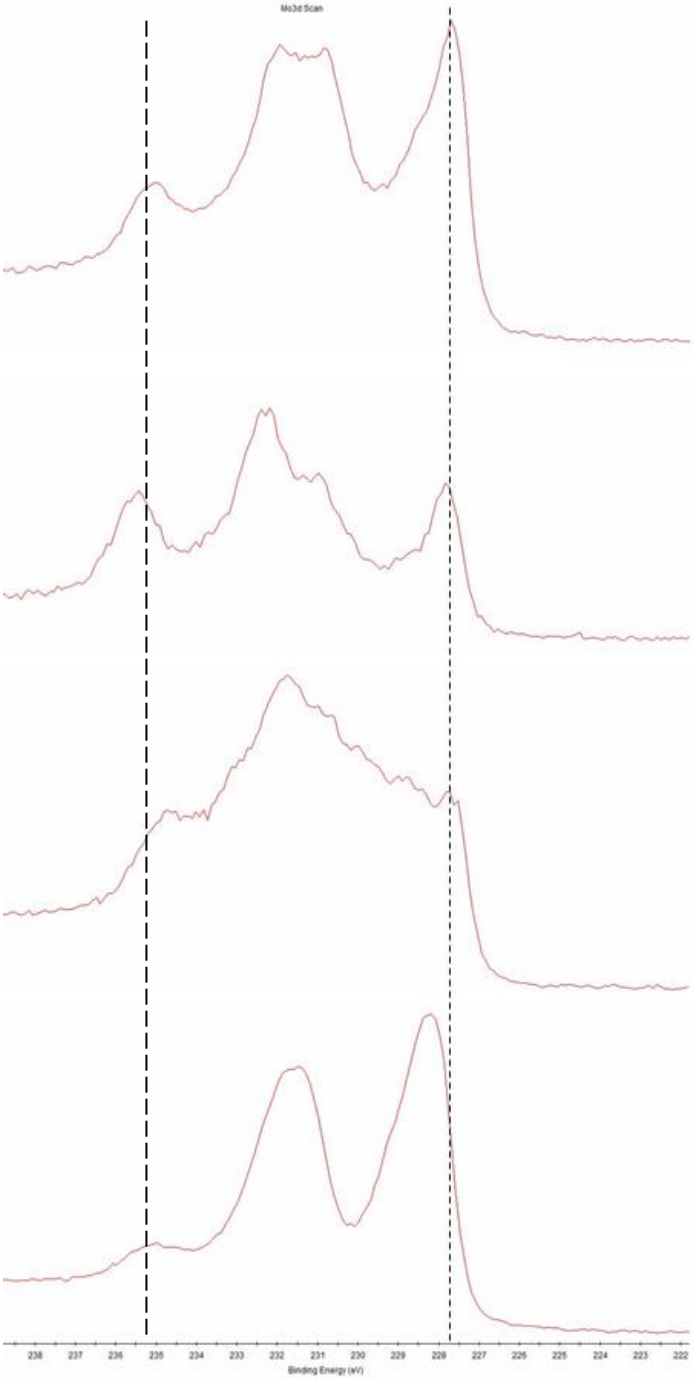

Figure 42: The Mo 3d spectra for as-prepared, plasma, heated, and heated-plasma 1:2 CoMo samples from top to bottom. The vertical lines represent expected positions of the Mo^0 $3d_{5/2}$ (227.8 eV) and $CoMoO_4$ $3d_{3/2}$ peaks

Unlike in the analysis by Biesinger et al. [53] as seen in Figure 33, it was necessary to begin the Shirley background further to the left past the $2p_{1/2}$ components. This is because the fitting algorithm considers peaks with significant portions found outside the range of the background as a poor fit; and attempts to eliminate these peaks. This causes chemical states that fit well but include longer tails to be erroneously removed. By starting the background at a higher binding energy, as shown in Figure 43, the presence of a tail does not increase the error. However, since each spectrum has somewhat unique features, the background had to begin at different positions to provide a reasonable amount of space. Since a minor change in the starting point leads to a significant difference in the calculated composition, this procedure introduces a considerable amount of error. Nonetheless, it is evident that the heated-plasma samples contained a substantial amount of elemental Fe as its peak at 706.6 eV [53] towers above the rest of the signal, as shown in Figure 44. According to the model, 40-60% of iron is in this form; as opposed to the specimens subjected to different conditions whose spectra contained no distinct peaks, with the highest calculated amount to be 5.8%. Interestingly, two of the heated-plasma spectra suggest relatively low amounts of elemental iron: 25.3% and 11.4%. The other spot on the same samples were found to contain 58.5% and 50.7% elemental iron. This is likely due to the surface being heterogeneous, with its sensitivity to the environment being greater in some areas. This possibility will be explored in the SEM section.

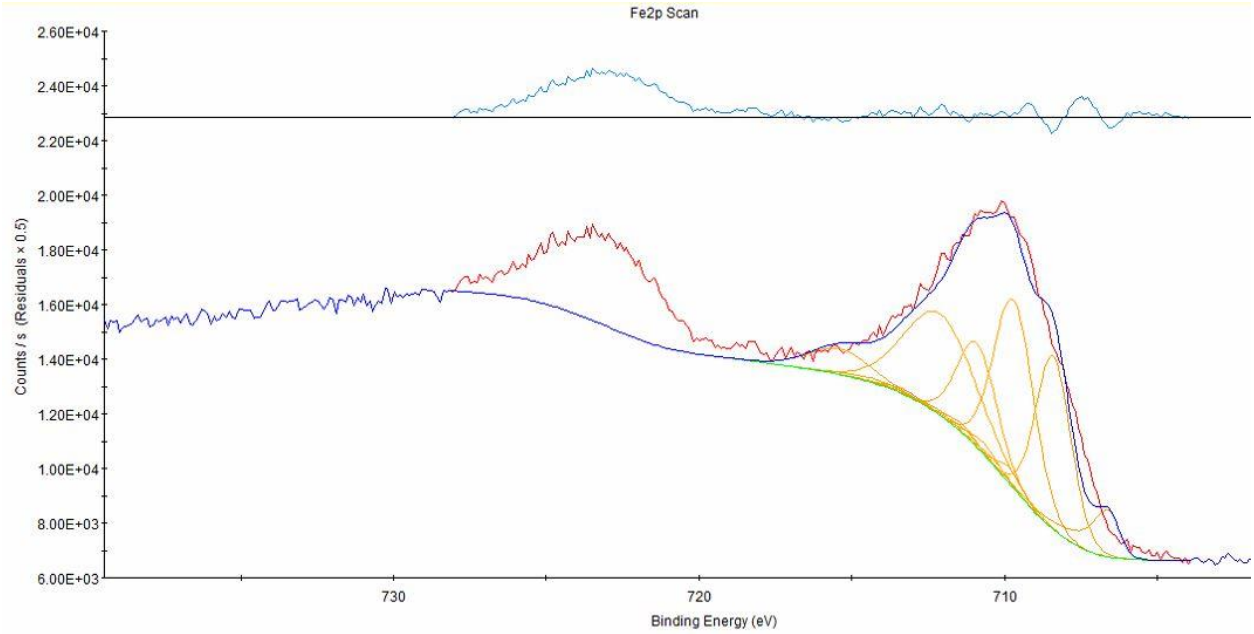

Figure 43: Fitted Fe 2p spectrum of a 2:1 heated FeRu sample.

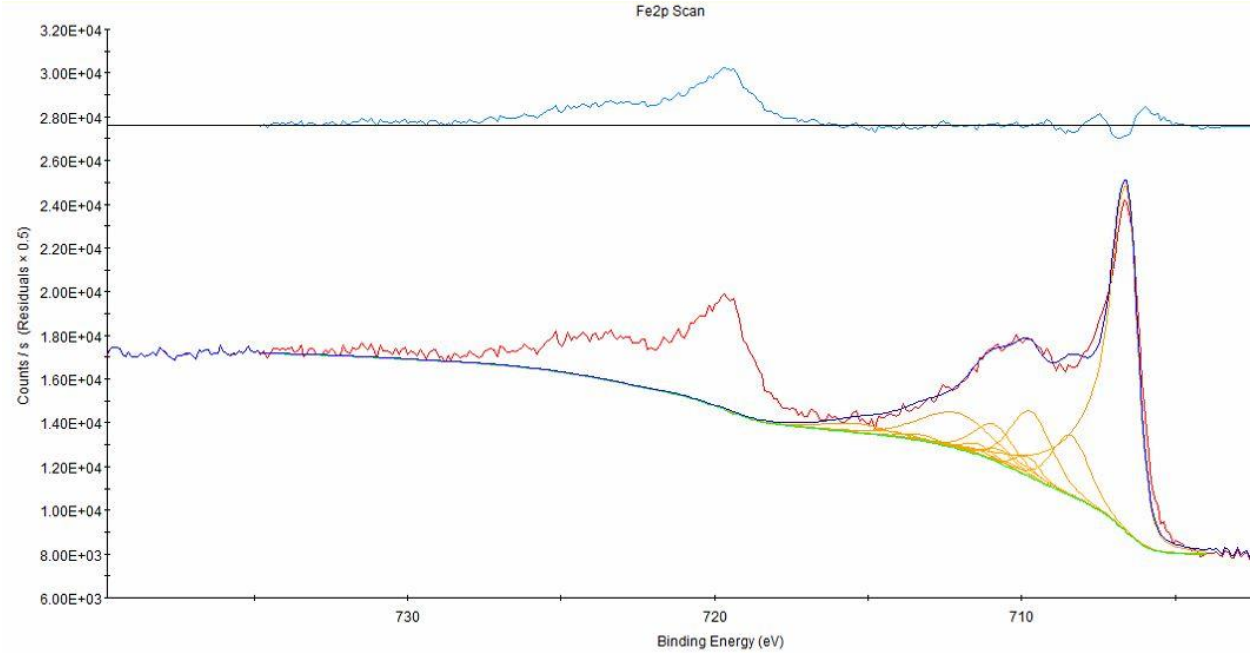

Figure 44: Fitted Fe 2p spectrum of a 2:1 heated-plasma FeRu sample.

Figure 45 shows the calculated proportion of iron, based on the average across all Fe:Ru ratios, in each chemical state; with the error bars representing the standard deviation. The error is especially high for FeO and Fe_3O_4 species, indicating that it is likely that the algorithm has difficulty differentiating between the two oxides. It can be concluded however that all samples except the heated-plasma ones consist mainly of oxides. When heat is applied, the Fe_3O_4 percentage drops below 5% whereas the amount of FeO remains significant. The amount of FeOOH consistently accounts for nearly 10% of the iron found.

When performing survey scans, sulfur was detected in several samples; ranging from 2-9% of the atomic percentage as calculated by the Avantage survey-analysis function. A scan taken of the sulfur region for the 2:1 NiRu heated-plasma is presented in Figure 46, clearly showing the presence of S. According to a colleague, the XPS is used by researchers to determine the purity of salts that contain sulphates, which can sublimate on the BNNT sample under ultra-high vacuum. This is believed to be the case since no sources of sulfur contamination were discovered from an investigation of equipment used to synthesize and modify the samples.

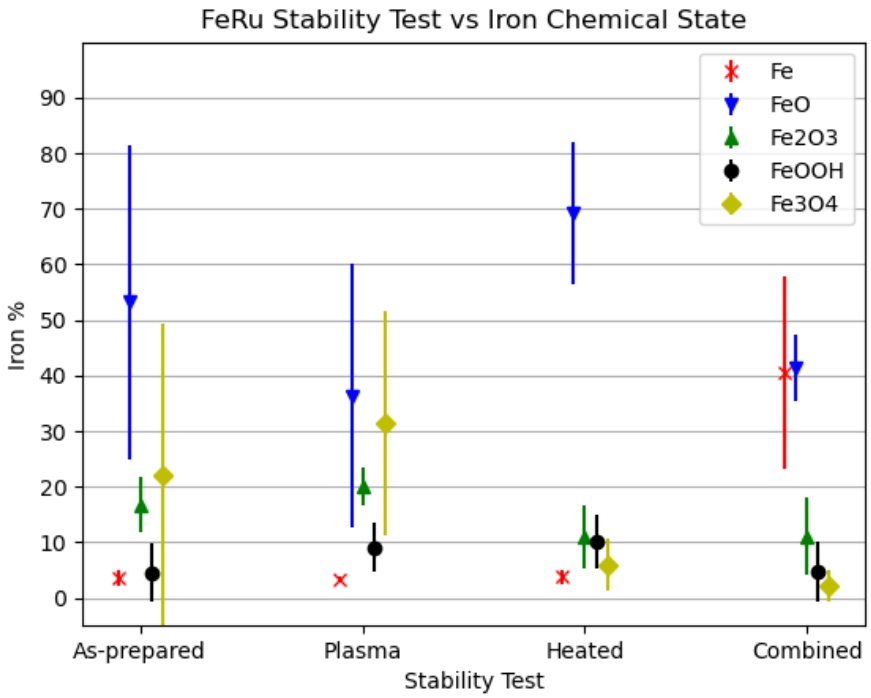

Figure 45: The proportion of iron found in various chemical states for each stability test. The error bars represent the standard deviation.

In the following section on inductively coupled plasma atomic emission spectroscopy (ICP-AES), the presence of sulfur will be verified. Since the sulfur peaks do not overlap with peaks of any of the metals used in this study, the peak fitting process was not impeded. However, a layer of contamination is known to obstruct photons with a high binding energy [48], so it is possible that nickel, iron and cobalt, elements with moderate binding energies had their peak areas slightly reduced. Adventitious carbon, a thin layer of carbon that results from exposure to air, may also contribution to this effect. Carbon can be removed by operating the ion gun before analyzing samples with the XPS. This was not done however, as parts of the oxide layer will also be etched away. In future studies, the risk of sulfur contamination can be reduced by operating the XPS after workers whose samples do not contain sulphates.

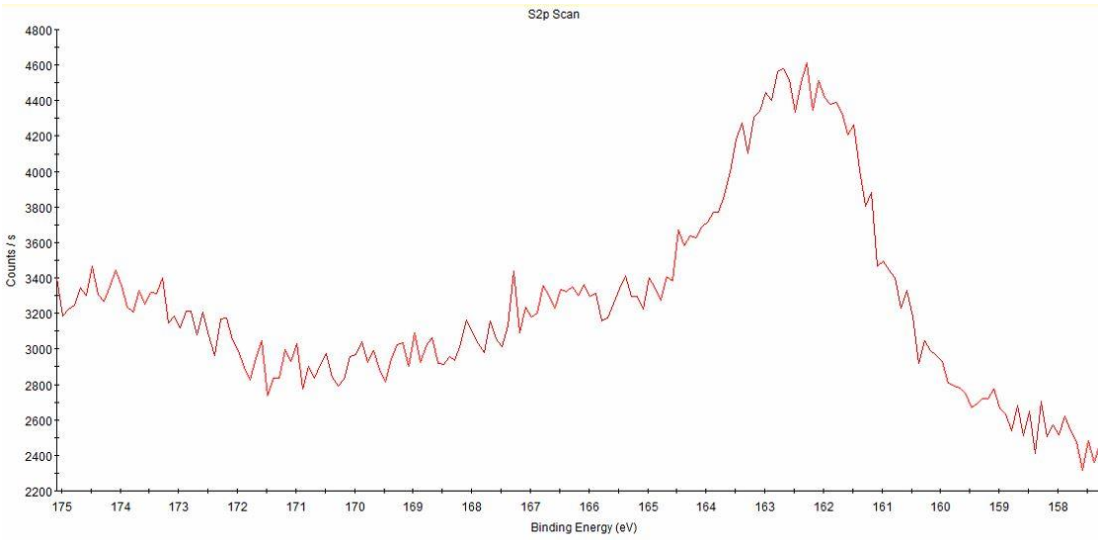

Figure 46: A S 2p peak found in the 2:1 NiRu heated-plasma sample.

In calculating the composition of the surface, the peak fitting software uses sensitivity factor S, which relates peak area to relative concentrations defined as [48]:

$$S = f\sigma\theta y\lambda AT$$

where f is the x-ray flux, σ is the photoelectric cross section, θ is a factor that depends on the specific instrument used, y is the efficiency of photoelectron formation, λ is the mean free path of the photoelectrons, A is the surface area analyzed, and T is the detection efficiency. The number of atoms of a certain element in a sample is [48]:

$$n = \frac{I}{S}$$

where I is the number of photoelectrons measured. Moulder et al. [48] expects that using this method would provide semi-quantitative results that are accurate within 10-20%. It is noted however that the error increases for heterogenous samples; which was confirmed in my analysis when two spots on the same sample had significantly different spectra and thus different chemical states. Additionally, first row transition metals (Fe, Co, Ni) generally have nonuniform y values that are dependent on the chemical state. This is another source of error since Avantage uses a single y value for each element.

Inductively Coupled Plasma Atomic Emission Spectroscopy

The energy required to vaporize a metal in terms of a unit of mass is the sum of the amount needed to raise its temperature to its boiling point, and additional energy consumed in phase changes based on its heats of fusion and vaporization. This value, the total ablation energy, is the minimum energy required. Based only on these values, it is expected that the ablation rates should differ by no more than 20%. However, much more energy is consumed due to thermal conduction with the bulk, ionization, and conversion to KE, factors that do not scale proportionally with the total ablation energy. With the fluence and wavelength constant, it is thought that the difference in fractional ionization across the metals is influenced most by the melting points and first ionization energies [35]. Thermal conduction is proportional to the thermal diffusivity, which varies significantly across metals. Tables 2 and 3 shows the thermal properties of each metal considered.

The ICP-AES results for filter paper samples with FeRu, CoMo and NiRu coatings are shown in Figure 47. The amount of metal deposited per laser pulse is the slope of the best-fit line as presented in Table 7. The relationship between the number of laser shots and the amount deposited appears linear only for FeRu. For NiRu, less metal is deposited per pulse with the highest number of shots, with the opposite being the case for CoMo. The mass ratio of each metal is the most consistent for CoMo with the ratio ranging from 0.75-0.82. This is moderately consistent with their total ablation energies, which suggests the value should be 0.88. This value likely shifted up due to the first ionization energy of Co (in units of MJ/kg) being 1.8 times that of Mo. This suggests that the ionization energy is more important than the melting point in determining fractional ionization, as the melting point of Mo is 855˚C higher than that of Co. A similar explanation can be made for FeRu with a theoretical value of 0.93; with the experimental ratio staying near 0.85 except for the 200-shot sample at 1.61. NiRu, however shows the opposite, with an experimental value ranging from 0.64-0.94 compared to a theoretical value of 0.99. The first ionization energy of Ni is close to double that of Ru, suggesting that the theoretical value should be lower. An explanation involving the thermal diffusivity of Ru being much higher than Ni can be ruled out since the value for Fe is similar to that of Ni. These results demonstrate that while the ratios of the total ablation energies can be used as a reasonable estimation for the deposition ratios, the true value is difficult to predict as many factors are involved. A first step would be to increase the sample size to reduce error due to variability.

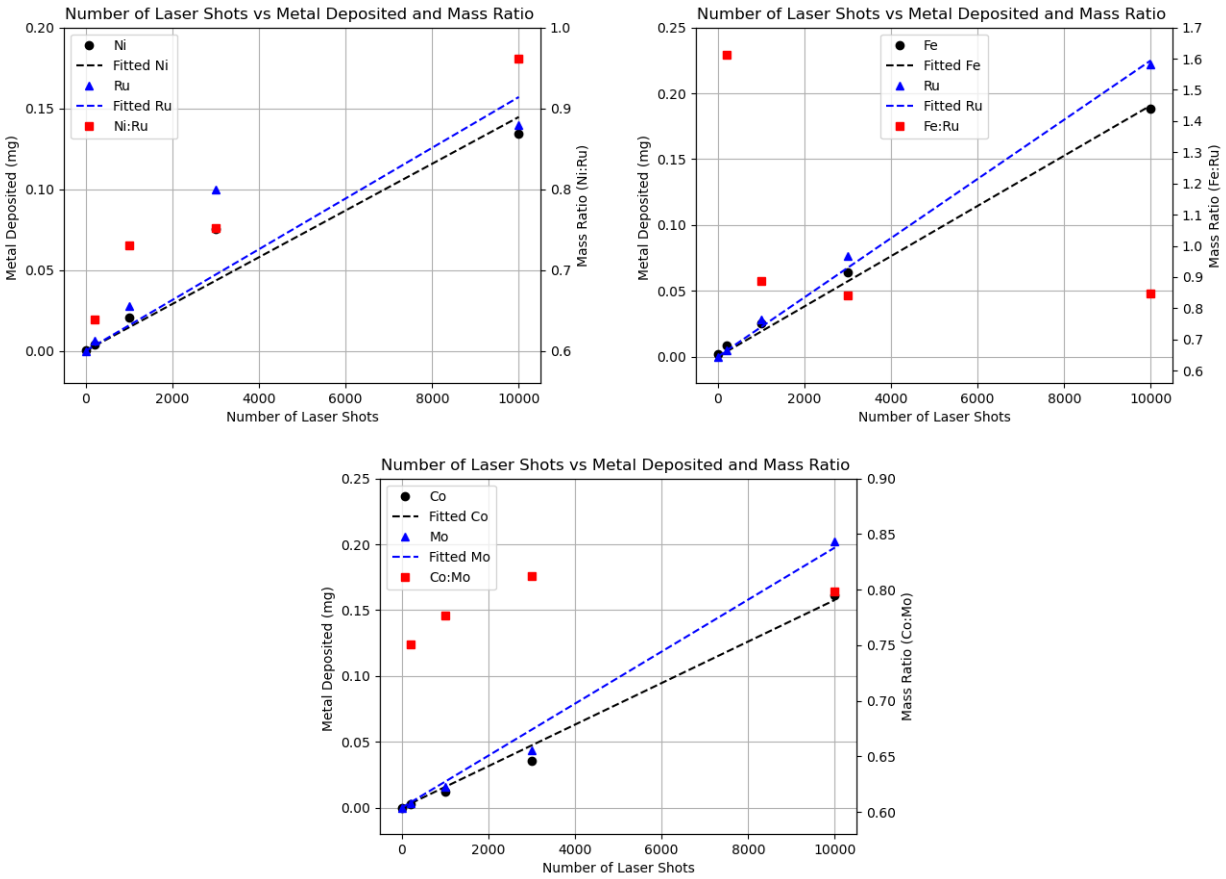

Figure 47: The number of laser shots plotted against the amount of metal deposited for NiRu (top left), FeRu (top right), and CoMo (bottom).

Sample	Metal	Mass Deposited per Laser Pulse (ng)
NiRu	Ni	14.5
	Ru	15.7
FeRu	Fe	19.1
	Ru	22.5
CoMo	Co	15.8
	Mo	19.8

Table 7: The amount of metal deposited per laser pulse based on the best-fit line.

In each case, the actual ablation energy is three orders of magnitude higher than the theoretical amount when considering the laser's input energy of 185 mJ/pulse, indicating a high degree of energy loss. It is believed that the largest fraction of energy is consumed in the ionization of the metals, which are ejected with high KEs. Other factors contributing to this energy loss include losses due to the laser's angle of incidence, the reflectivity of the mirrors and lens, the targets' surface roughness and parts of the plume expanding beyond the substrate.

Since XPS spectra previous suggested the presence of sulfur, ICP-AES is used to quantify the amount found in FeRu and NiRu filter paper, and NiRu BNNT samples. Table 8 shows the results. All specimens are found to contain a small amount of sulfur. For filter paper samples, PLD slightly increases the wt %, which on the other hand increases by over a factor of three for the BNNT specimens. The coated BNNT samples were previously tested using the XPS and may have gained additional sulfur in the process. Since sulfur is present on blank substrates, this eliminates the possibility of sulfur contamination solely from the PLD chamber or the reactor used in stability tests. The source of sulfur is yet to be found.

Substrate	Metals	Number of Laser Shots	Stability Test	Sulfur wt %
Filter Paper	None (blank)	0	As-prepared	0.0144
	NiRu	200		0.0183
	NiRu	1000		0.0179
	NiRu	3000		0.0192
	NiRu	10000		0.0179
	FeRu	200		0.0201
	FeRu	1000		0.0179
	FeRu	3000		0.0168
	FeRu	10000		0.0192
BNNT	None (blank)	0		0.0272
	NiRu	1000:2000		0.0838
	NiRu	1000:2000	Plasma	0.0930
	NiRu	1000:2000	Heated-Plasma	0.1698*

*Low degree of confidence due to high relative standard deviation

Table 8: Sulfur wt % of each sample according to ICP-AES study.

Scanning Electron Microscopy

SEM images of BNNT samples coated with FeRu, CoMo and NiRu with resolutions ranging from 100 nm - 10 μm are analyzed to compare the morphologies of as-prepared samples to ones heated and plasma-treated. Before examining images showing individual nanotubes, it is important to note the variability across the surface. Figure 48 (left) shows an as-prepared 1:1 FeRu sample with a resolution of 10μm. BNNTs are clearly visible in most of the image. However, to the top right, a solid mass can be seen. This is thought to be hexagonal-boron nitride (hBN), an undesirable substance that is incorporated during the synthesis of BNNT buckypaper When comparing the lighter region to the top left with the dark area immediately to the right, it is evident that the surface is not smooth. Depending on the angle at which the photoelectrons are detected, it is possible that the ones originating from troughs would lose energy while travelling through the areas with a higher elevation before reaching the detector. Furthermore, hBN clusters seem to be closest to the sensor. These observations likely account for much of the differences in the XPS spectra found between two spots on the same sample. The differences are much greater in the heated FeRu sample as shown in Figure 48 (right). A crust-like formation, where individual nanotubes are no longer well-defined, is found on the right side of the image. This only occurs in limited sections of the surface, most of which looking like the left side of the image. Figure 49 (top) shows a higher resolution of the left side and Figure 49 (bottom) shows the crust-like

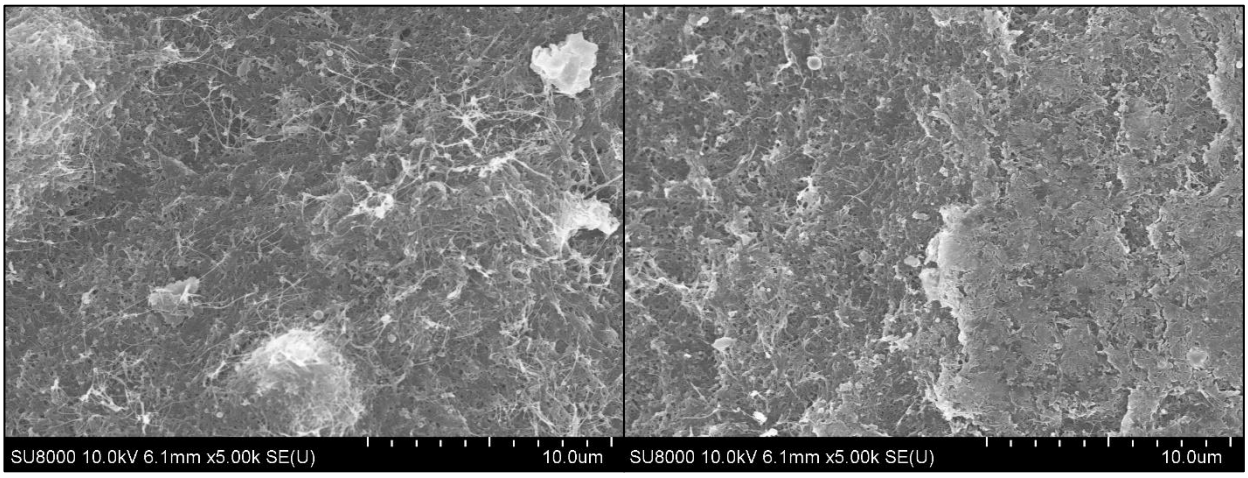

Figure 48: SEM images of 1:1 FeRu as-prepared (left) and heated (right) samples with a resolution of 10μm. The latter image showing the presence of a crust-like formation.

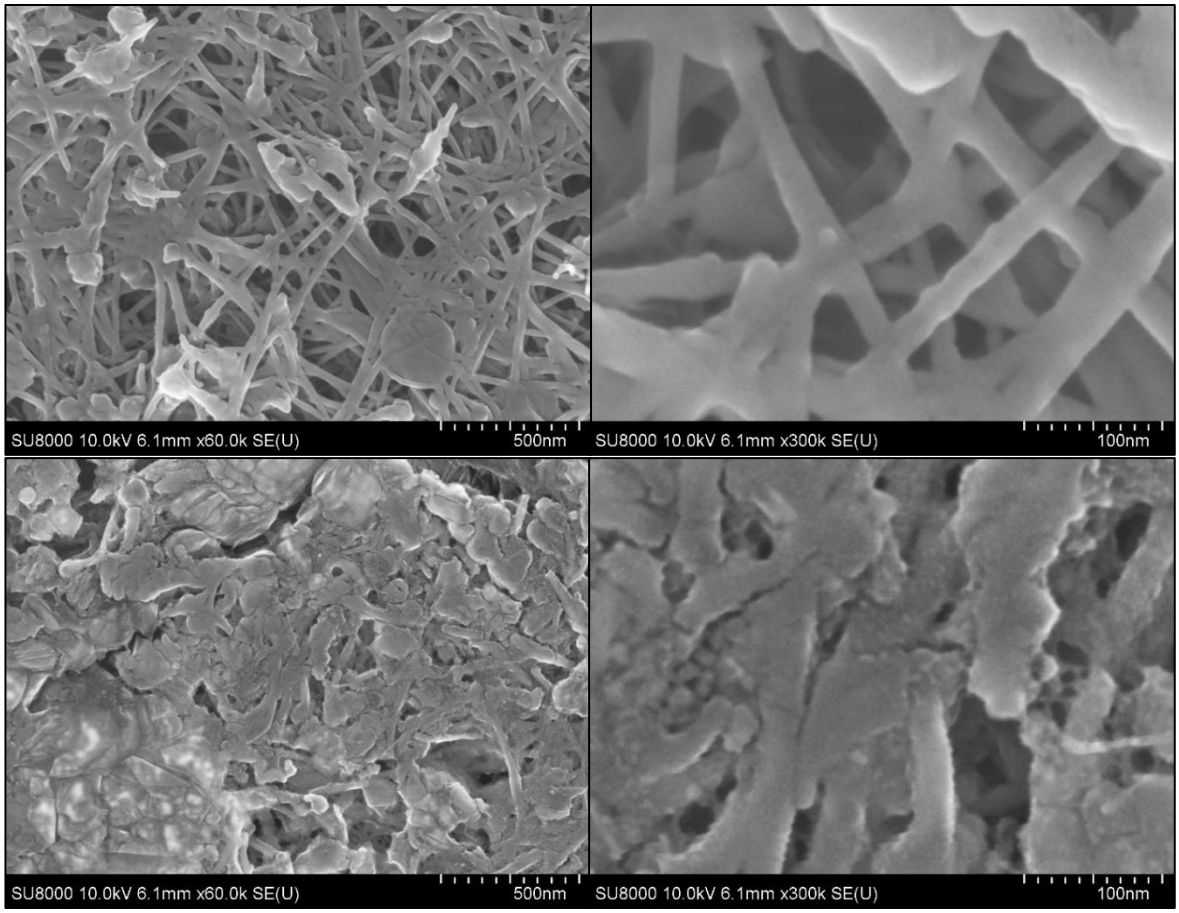

Figure 49: Higher resolution SEM images of 1:1 FeRu as-prepared (top) and heated (bottom) samples showing the reduction in surface area due to the crust-like formation.

formation, which undoubtably increases the surface area of the catalyst, reducing performance. Since BNNTs are known to be stable in air up to 900°C [23], it is believed that this change is due to migration of metal that was previously attached to the BNNT. XPS data suggested a large reduction of Fe_2O_3 and Fe_3O_4 in samples with heat, or heat and plasma applied. This agrees Tiernan et al. whose temperature-programmed reduction (TPR) profile shows a rapid increase in the rate of reduction of both of these oxides above 450°C. It is believed that they didn't form after re-exposure to air because the crust-like formation has a low surface area; and that much of the elemental Fe was not in contact with air. While the image obtained for the heated-plasma sample did not show this formation, it is expected that it will be more prevalent.

The surface of the heated CoMo sample was searched extensively but no abnormal regions were found. This may explain the similar amount of CoO and $CoMoO_4$ found between as-prepared, and heated samples since any reduction may be reversed upon exposure to air. The decrease in

elemental Co may be from oxidation with adsorbed water. Figure 50 shows the morphology that is typical to this specimen. The heated-plasma CoMo sample's surface appears to contain both morphologies as shown in Figure 51 with the latter having less defined BNNTs and providing an environment that is the most conducive for the presence of elemental Co.

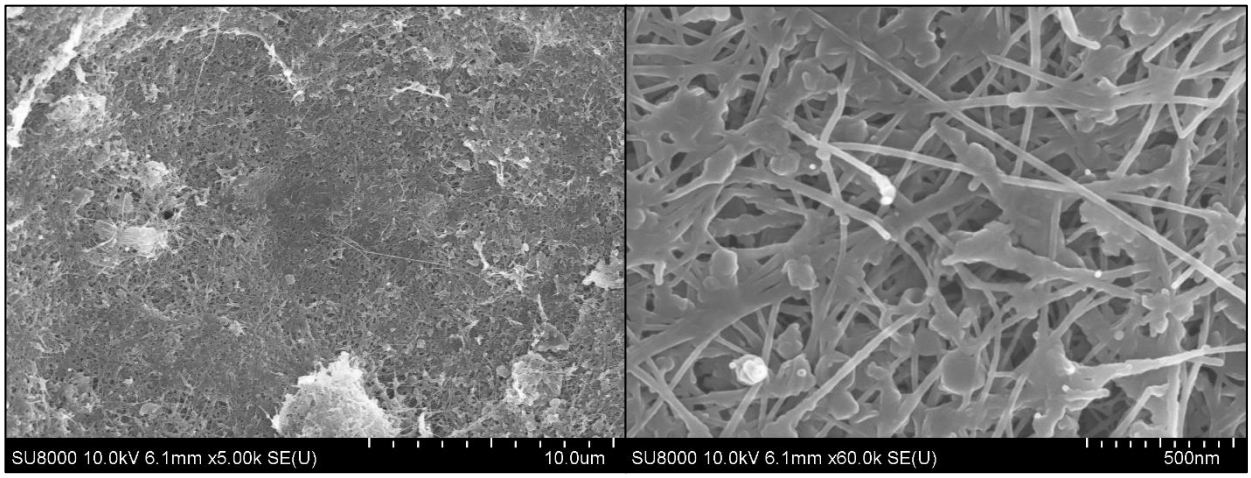

Figure 50: SEM images of a 1:1 CoMo heated sample with a high (right) and low (left) resolutions.

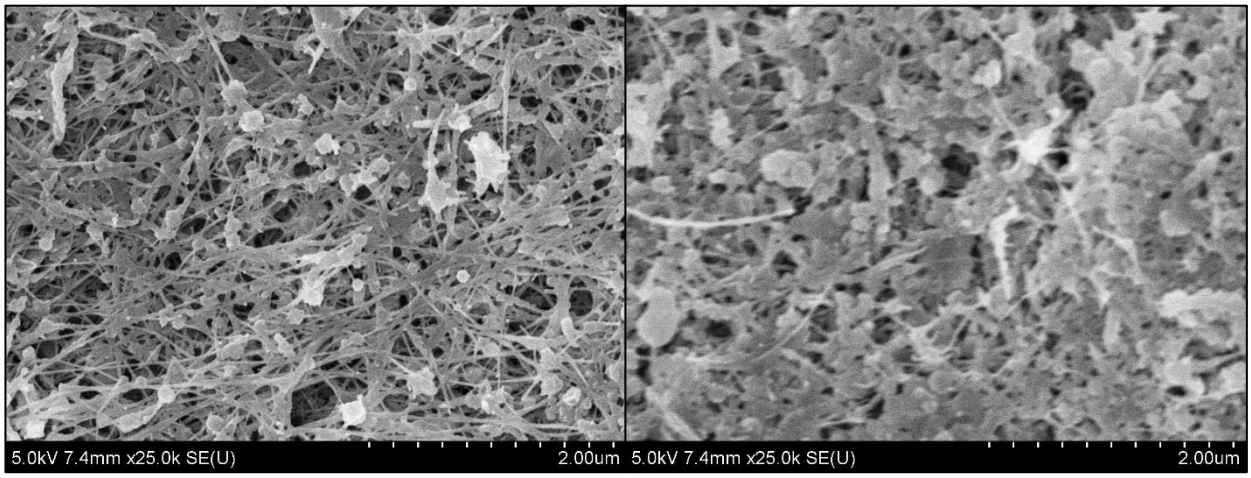

Figure 51: SEM images of a 1:1 CoMo plasma-heated sample with a section of the surface with a typical morphology (left) and one that exhibits a crust-like formation (right).

The samples exposed only to plasma have no visible change. In the above figures, the deposition of NPs causes the BNNTs to become thicker with fuzzy edges. Nanotubes that are found deeper seem to have less metal deposited. Since there are no other features that assist with distinguishing between NPs and BNNTs, it is not possible to determine the particle size. However, looking at these images it is believed that with 3000 laser shots applied, there is a continuous coating of metal along the surfaces of the nanotubes rather an individual NPs.

Conclusion

Plasma-catalytic ammonia synthesis is a promising alternative to the Haber-Bosch process since it can be powered with renewable sources that are intermittent in nature. It is commonly believed that several bimetallic combinations are effective; but none have been synthesized in the form of NPs. In this work, CoMo, FeRu and NiRu catalysts are synthesized on BNNT supports using PLD, a method that is thought to produce catalysts that are more stable than ones made using wet chemistry. An automated PLD system that includes substrate spinning for uniform deposition and a mechanism to switch between metal targets was implemented for this purpose.

XPS analysis of these samples was done to assess the variability across samples and the chemical states of the metal coatings. A comparison is made between as-prepared samples, samples heated to 500˚C (FeRu and CoMo) or 415˚C (NiRu), plasma-treated samples and ones exposed to both plasma and heat simultaneously. It is concluded that all metals except ruthenium are found predominantly in oxide forms in as-prepared, heated, and plasma-treated samples. Specimens subjected to a simultaneous application of heat and plasma contain higher quantities of elemental metal. While SEM images of as-prepared and plasma-treated samples show clearly distinguished nanotubes on the surface, heated and heated-plasma samples exhibit crust-like formations which are likely a result of migration of the metal coating. This results in a reduction of surface area and it is thought that metal oxides that were reduced during the stability test are no longer exposed to air upon removal from the reactor, thus remaining in elemental form. Two spots on the surface of the same sample sometimes produce a different XPS spectra. This is due to the heterogeneous nature of the surfaces, an effect that is compounded in treated samples with the emergence of a crust-like formation; something that is only seen in pockets across the surface.

The relationship between laser shots and metal deposited was established using ICP-AES. The FeRu plot suggests a linear relation, whereas for NiRu it appears that less metal is deposited per laser shot at higher loadings with the case being the opposite for CoMo. It is also found that the ratio between metals deposited can be moderately predicted by their thermal properties. Metals that require more energy to ablate generally deposit slower, and a high thermal diffusivity supports faster ablation. While the ratio between each metal deposited is largely constant, notable outliers are found. It is unclear if this is due to the specific shot count or to sample variability. Sulfur

contamination was found on all samples (CoMo was not measured) including blanks, agreeing with XPS findings. The source is currently unknown.

Recommendations

The next step in characterizing the samples would be to perform transmission electron microscopy (TEM) to determine the metal NP sizes. This can be used to determine the maximum loading possible without a significant increase in surface area as currently, the loading of each metal is no more than 0.25 wt % with 5000 laser shots of each metal. A much higher loading is likely necessary for the catalysts to have high activities. If the reactor for plasma-catalytic synthesis operates at a high temperature, more SEM imaging can be done to determine the threshold temperature for the emergence of the crust-like formation and the percentage of the surface that is covered by it. Finally, plasma-catalytic synthesis can be performed using the bimetallic catalysts to determine and compare the catalyst activities of various combinations and loadings.

The relationship between laser shots and metal deposited can be better understood by synthesizing more samples; namely by duplicating the previously used samples to determine the variability and by applying between 3000 and 10000 laser shots to establish whether the slope is linear. A further investigation can be done to determine the source of sulfur contamination.

References

[1] K. H. R. Rouwenhorst, Y. Engelmann, K. van ‘t Veer, R. S. Postma, A. Bogaerts, and L. Lefferts, “Plasma-driven catalysis: green ammonia synthesis with intermittent electricity,” *Green Chemistry*, vol. 22, no. 19, pp. 6258–6287, 2020, doi: 10.1039/d0gc02058c.

[2] U.S. Department of Energy, “HYDROGEN STRATEGY Enabling A Low-Carbon Economy,” Jul. 2020. Accessed: Jul. 10, 2022. [Online]. Available: https://www.energy.gov/sites/prod/files/2020/07/f76/USDOE_FE_Hydrogen_Strategy_July2020.pdf

[3] F. Gorky, A. Best, J. Jasinski, B. J. Allen, A. C. Alba-Rubio, and M. L. Carreon, “Plasma catalytic ammonia synthesis on Ni nanoparticles: The size effect,” *Journal of Catalysis*, vol. 393, pp. 369–380, Jan. 2021, doi: 10.1016/j.jcat.2020.11.030.

[4] C. Smith, A. K. Hill, and L. Torrente-Murciano, “Current and future role of Haber–Bosch ammonia in a carbon-free energy landscape,” *Energy & Environmental Science*, vol. 13, no. 2, pp. 331–344, Feb. 2020, doi: 10.1039/C9EE02873K.

[5] C. J. H. Jacobsen, S. Dahl, B. S. Clausen, S. Bahn, A. Logadottir, and J. K. Nørskov, “Catalyst Design by Interpolation in the Periodic Table: Bimetallic Ammonia Synthesis Catalysts,” *Journal of the American Chemical Society*, vol. 123, no. 34, pp. 8404–8405, Aug. 2001, doi: 10.1021/ja010963d.

[6] M. A. McArthur, L. Jorge, S. Coulombe, and S. Omanovic, “Synthesis and characterization of 3D Ni nanoparticle/carbon nanotube cathodes for hydrogen evolution in alkaline electrolyte,” *Journal of Power Sources*, vol. 266, pp. 365–373, Nov. 2014, doi: 10.1016/j.jpowsour.2014.05.036.

[7] A. von Keudell and V. Schulz-von der Gathen, “Foundations of low-temperature plasma physics—an introduction,” *Plasma Sources Science and Technology*, vol. 26, no. 11, p. 113001, Oct. 2017, doi: 10.1088/1361-6595/aa8d4c.

[8] M. L. Carreon, “Plasma catalysis: a brief tutorial,” *Plasma Research Express*, vol. 1, no. 4, p. 043001, Nov. 2019, doi: 10.1088/2516-1067/ab5a30.

[9] H.-H. Kim, Y. Teramoto, A. Ogata, H. Takagi, and T. Nanba, “Plasma Catalysis for Environmental Treatment and Energy Applications,” *Plasma Chemistry and Plasma Processing*, vol. 36, no. 1, pp. 45–72, Oct. 2015, doi: 10.1007/s11090-015-9652-7.

[10] H.-H. Kim, Y. Teramoto, A. Ogata, H. Takagi, and T. Nanba, “Atmospheric-pressure nonthermal plasma synthesis of ammonia over ruthenium catalysts,” *Plasma Processes and Polymers*, vol. 14, no. 6, p. 1600157, Oct. 2016, doi: 10.1002/ppap.201600157.

[11] K. H. R. Rouwenhorst, H.-H. Kim, and L. Lefferts, “Vibrationally Excited Activation of N2 in Plasma-Enhanced Catalytic Ammonia Synthesis: A Kinetic Analysis,” *ACS Sustainable Chemistry & Engineering*, vol. 7, no. 20, pp. 17515–17522, Sep. 2019, doi: 10.1021/acssuschemeng.9b04997.

[12] “Bond Energy | Chemistry for Non-Majors,” *Lumenlearning.com*, 2020. https://courses.lumenlearning.com/cheminter/chapter/bond-energy/ (accessed May 20, 2021).

[13] P. Peng, Y. Li, Y. Cheng, S. Deng, P. Chen, and R. Ruan, “Atmospheric Pressure Ammonia Synthesis Using Non-thermal Plasma Assisted Catalysis,” *Plasma Chemistry*

and Plasma Processing, vol. 36, no. 5, pp. 1201–1210, Jun. 2016, doi: 10.1007/s11090-016-9713-6.

[14] J. Hong, S. Pancheshnyi, E. Tam, J. J. Lowke, S. Prawer, and A. B. Murphy, "Kinetic modelling of NH_3production in N_2–H_2non-equilibrium atmospheric-pressure plasma catalysis," *Journal of Physics D: Applied Physics*, vol. 50, no. 15, p. 154005, Mar. 2017, doi: 10.1088/1361-6463/aa6229.

[15] T. Mizushima, K. Matsumoto, J. Sugoh, H. Ohkita, and N. Kakuta, "Tubular membrane-like catalyst for reactor with dielectric-barrier-discharge plasma and its performance in ammonia synthesis," *Applied Catalysis A: General*, vol. 265, no. 1, pp. 53–59, Jun. 2004, doi: 10.1016/j.apcata.2004.01.002.

[16] P. Mehta *et al.*, "Overcoming ammonia synthesis scaling relations with plasma-enabled catalysis," *Nature Catalysis*, vol. 1, no. 4, pp. 269–275, Apr. 2018, doi: 10.1038/s41929-018-0045-1.

[17] J. Nakajima and H. Sekiguchi, "Synthesis of ammonia using microwave discharge at atmospheric pressure," *Thin Solid Films*, vol. 516, no. 13, pp. 4446–4451, May 2008, doi: 10.1016/j.tsf.2007.10.053.

[18] S. X. Huang, T. S. Rufael, and J. L. Gland, "Diimide formation on the Ni(100) surface," *Surface Science*, vol. 290, no. 1–2, pp. L673–L676, Jun. 1993, doi: 10.1016/0039-6028(93)90578-8.

[19] C. D. Zeinalipour-Yazdi, J. S. J. Hargreaves, and C. R. A. Catlow, "Low-T Mechanisms of Ammonia Synthesis on Co3Mo3N," *The Journal of Physical Chemistry C*, vol. 122, no. 11, pp. 6078–6082, Jan. 2018, doi: 10.1021/acs.jpcc.7b12364.

[20] C. Shi, S. Wang, X. Ge, S. Deng, B. Chen, and J. Shen, "A review of different catalytic systems for dry reforming of methane: Conventional catalysis-alone and plasma-catalytic system," *Journal of CO2 Utilization*, vol. 46, p. 101462, Apr. 2021, doi: 10.1016/j.jcou.2021.101462.

[21] K. Aika, J. Kubota, Y. Kadowaki, Y. Niwa, and Y. Izumi, "Molecular sensing techniques for the characterization and design of new ammonia catalysts," *Applied Surface Science*, vol. 121–122, pp. 488–491, Nov. 1997, doi: 10.1016/s0169-4332(97)00343-7.

[22] J. K. Kim *et al.*, "Synthesis of Boron Nitride Nanotubes Incorporated with Pd and Pt Nanoparticles for Catalytic Oxidation of Carbon Monoxide," *Industrial & Engineering Chemistry Research*, vol. 58, no. 43, pp. 20154–20161, Oct. 2019, doi: 10.1021/acs.iecr.9b03954.

[23] K. S. Kim and T. H. Kim, "Nanofabrication by thermal plasma jets: From nanoparticles to low-dimensional nanomaterials," *Journal of Applied Physics*, vol. 125, no. 7, p. 070901, Feb. 2019, doi: 10.1063/1.5060977.

[24] K. S. Kim *et al.*, "Scalable manufacturing of boron nitride nanotubes and their assemblies: a review," *Semiconductor Science and Technology*, vol. 32, no. 1, p. 013003, Dec. 2016, doi: 10.1088/0268-1242/32/1/013003.

[25] R. Arenal, M.-S. Wang, Z. Xu, A. Loiseau, and D. Golberg, "Young modulus, mechanical and electrical properties of isolated individual and bundled single-walled boron nitride nanotubes," *Nanotechnology*, vol. 22, no. 26, p. 265704, May 2011, doi: 10.1088/0957-4484/22/26/265704.

[26] K. S. Kim *et al.*, "Hydrogen-catalyzed, pilot-scale production of small-diameter boron nitride nanotubes and their macroscopic assemblies," *ACS nano*, vol. 8, no. 6, pp. 6211–6220, Jun. 2014, doi: 10.1021/nn501661p.

[27] E. Irissou, F. Vidal, T. Johnston, M. Chaker, D. Guay, and A. N. Ryabinin, "Influence of an inert background gas on bimetallic cross-beam pulsed laser deposition," *Journal of Applied Physics*, vol. 99, no. 3, p. 034904, Feb. 2006, doi: 10.1063/1.2165412.
[28] R. Eason, *Pulsed laser deposition of thin films : applications-led growth of functional materials*. Hoboken, N.J.: Wiley-Interscience, 2007.
[29] B. N. Chichkov, C. Momma, S. Nolte, F. Alvensleben, and A. Tünnermann, "Femtosecond, picosecond and nanosecond laser ablation of solids," *Applied Physics A Materials Science & Processing*, vol. 63, no. 2, pp. 109–115, Aug. 1996, doi: 10.1007/bf01567637.
[30] R. Heid, "Electron-phonon Coupling," *The physics of correlated insulators, metals, and superconductors*, vol. 7, 2017.
[31] M. Kim, S. Osone, T. Kim, H. Higashi, and T. Seto, "Synthesis of Nanoparticles by Laser Ablation: A Review," *KONA Powder and Particle Journal*, vol. 34, no. 0, pp. 80–90, 2017, doi: 10.14356/kona.2017009.
[32] S. Preuss, A. Demchuk, and M. Stuke, "Sub-picosecond UV laser ablation of metals," *Applied Physics A Materials Science & Processing*, vol. 61, no. 1, pp. 33–37, Jul. 1995, doi: 10.1007/bf01538207.
[33] "Index of Elements," *periodictable.com*. https://periodictable.com/Elements (accessed May 21, 2022).
[34] L. Torrisi, S. Gammino, L. Andò, V. Nassisi, D. Doria, and A. Pedone, "Comparison of nanosecond laser ablation at 1064 and 308 nm wavelength," *Applied Surface Science*, vol. 210, no. 3–4, pp. 262–273, Apr. 2003, doi: 10.1016/s0169-4332(02)01467-8.
[35] L. Torrisi, L. Andò, S. Gammino, J. Kràsa, and L. Làska, "Ion and neutral emission from pulsed laser irradiation of metals," *Nuclear Instruments and Methods in Physics Research Section B: Beam Interactions with Materials and Atoms*, vol. 184, no. 3, pp. 327–336, Nov. 2001, doi: 10.1016/s0168-583x(01)00790-x.
[36] W. Svendsen, O. Ellegaard, and J. Schou, "Laser ablation deposition measurements from silver and nickel," *Applied Physics A Materials Science & Processing*, vol. 63, no. 3, pp. 247–255, Sep. 1996, doi: 10.1007/bf01567877.
[37] B. Toftmann, J. Schou, and J. G. Lunney, "Dynamics of the plume produced by nanosecond ultraviolet laser ablation of metals," *Physical Review B*, vol. 67, no. 10, Mar. 2003, doi: 10.1103/physrevb.67.104101.
[38] S. Senkan, M. Kahn, S. Duan, A. Ly, and C. Leidholm, "High-throughput metal nanoparticle catalysis by pulsed laser ablation," *Catalysis Today*, vol. 117, no. 1–3, pp. 291–296, Sep. 2006, doi: 10.1016/j.cattod.2006.05.051.
[39] C. B. Arnold and M. J. Aziz, "Stoichiometry issues in pulsed-laser deposition of alloys grown from multicomponent targets," *Applied Physics A Materials Science & Processing*, vol. 69, no. S1, pp. S23–S27, Dec. 1999, doi: 10.1007/s003399900182.
[40] H. Krebs and O. Bremert, "Pulsed laser deposition of thin metallic alloys," *Applied Physics Letters*, vol. 62, no. 19, pp. 2341–2343, May 1993, doi: 10.1063/1.109412.
[41] R. K. Rai *et al.*, "Iron–Cobalt-Based Materials: An Efficient Bimetallic Catalyst for Ammonia Synthesis at Low Temperatures," *ACS Catalysis*, vol. 12, no. 1, pp. 587–599, Dec. 2021, doi: 10.1021/acscatal.1c05078.
[42] *Brilliant / BrilliantB Instruction Manual*. Quantel, 2002.
[43] D. Steck, *Classical and Modern Optics*. 2015.

[44] "Push-Pull Linear Feedthrough, NW16, Flange, 2' Travel," *MDC Precision*. https://www.mdcprecision.com/663012-push-pulllinearfeedthrough-nw16-flange-2-inchtravel (accessed May 23, 2021).
[45] "XSlide Motorized Translation Stages," *Velmex Motorized XSlide Systems*. https://www.velmex.com/Products/XSlide/XSlide-motorized.html. (accessed May 23, 2021).
[46] K. S. Kim *et al.*, "Polymer nanocomposites from free-standing, macroscopic boron nitride nanotube assemblies," *RSC Advances*, vol. 5, no. 51, pp. 41186–41192, 2015, doi: 10.1039/c5ra02988k.
[47] S. Walker, "A preliminary study on the use of boron nitride nanotubes as a support for non-thermal plasma catalytic assisted ammonia synthesis," McGill University Library, Dec. 2021. [Online]. Available: https://escholarship.mcgill.ca/concern/theses/zw12zb044?locale=en
[48] J. F. Moulder, W. F. Stickle, P. E. Sobol, and K. D. Bomben, *Handbook of X-ray Photoelectron Spectroscopy*. Perkin-Elmer Corporation, 1992.
[49] D. J. Morgan, "Resolving ruthenium: XPS studies of common ruthenium materials," *Surface and Interface Analysis*, vol. 47, no. 11, pp. 1072–1079, Sep. 2015, doi: 10.1002/sia.5852.
[50] "Carbon | XPS Periodic Table," *www.thermofisher.com*. https://www.thermofisher.com/ca/en/home/materials-science/learning-center/periodic-table/non-metal/carbon.html (accessed Apr. 21, 2022).
[51] D. R. Baer *et al.*, "XPS guide: Charge neutralization and binding energy referencing for insulating samples," *Journal of Vacuum Science & Technology A*, vol. 38, no. 3, p. 031204, May 2020, doi: 10.1116/6.0000057.
[52] G. H. Major *et al.*, "Practical guide for curve fitting in x-ray photoelectron spectroscopy," *Journal of Vacuum Science & Technology A*, vol. 38, no. 6, p. 061203, Dec. 2020, doi: 10.1116/6.0000377.
[53] M. C. Biesinger, B. P. Payne, A. P. Grosvenor, L. W. M. Lau, A. R. Gerson, and R. St. C. Smart, "Resolving surface chemical states in XPS analysis of first row transition metals, oxides and hydroxides: Cr, Mn, Fe, Co and Ni," *Applied Surface Science*, vol. 257, no. 7, pp. 2717–2730, Jan. 2011, doi: 10.1016/j.apsusc.2010.10.051.
[54] M. C. Biesinger, B. P. Payne, L. W. M. Lau, A. Gerson, and R. St. C. Smart, "X-ray photoelectron spectroscopic chemical state quantification of mixed nickel metal, oxide and hydroxide systems," *Surface and Interface Analysis*, vol. 41, no. 4, pp. 324–332, Apr. 2009, doi: 10.1002/sia.3026.
[55] R. L. Chin and D. M. Hercules, "Surface spectroscopic characterization of cobalt-molybdenum-alumina catalysts," *The Journal of Physical Chemistry*, vol. 86, no. 16, pp. 3079–3089, Aug. 1982, doi: 10.1021/j100213a008.
[56] E. De Vito and P. Marcus, "XPS study of passive films formed on molybdenum-implanted austenitic stainless steels," *Surface and Interface Analysis*, vol. 19, no. 1–12, pp. 403–408, Jun. 1992, doi: 10.1002/sia.740190175.
[57] N. S. McIntyre, D. D. Johnston, L. L. Coatsworth, R. D. Davidson, and J. R. Brown, "X-ray photoelectron spectroscopic studies of thin film oxides of cobalt and molybdenum," *Surface and Interface Analysis*, vol. 15, no. 4, pp. 265–272, Apr. 1990, doi: 10.1002/sia.740150406.